Nano Research

ISSN 1998-0124 CN 11-5974/O4
https://doi.org/10.26599/NR.2026.94909208

Research Article

High-entropy quantum dots-modulated Pt/MXene heterojunction nanozymes for targeted catalytic therapy of hepatocellular carcinoma

Xiaodong Xu[1,§], Xiancheng Liu[2,§], Weiwei Shao[3], Yong Qiang[4], Feiran Wang[5](✉)

[1] Department of General Surgery, The First People's Hospital of Yancheng, Yancheng 224000, China

[2] Department of Radiation Oncology, Affiliated Hospital of Nantong University, Nantong 226000, China

[3] Department of Hepatobiliary Surgery, Beijing Chao-Yang Hospital affiliated to Capital Medical University, Beijing 100023, China

[4] Department of Hepatobiliary Surgery, JingMen People's Hospital, Jingchu University of Technology Affiliated JingMen People's Hospital, JingMen 448000, China

[5] Department of General Surgery, Affiliated Hospital of Nantong University, Nantong 226000, China

[§] Xiaodong Xu and Xiancheng Liu contributed equally to this work.

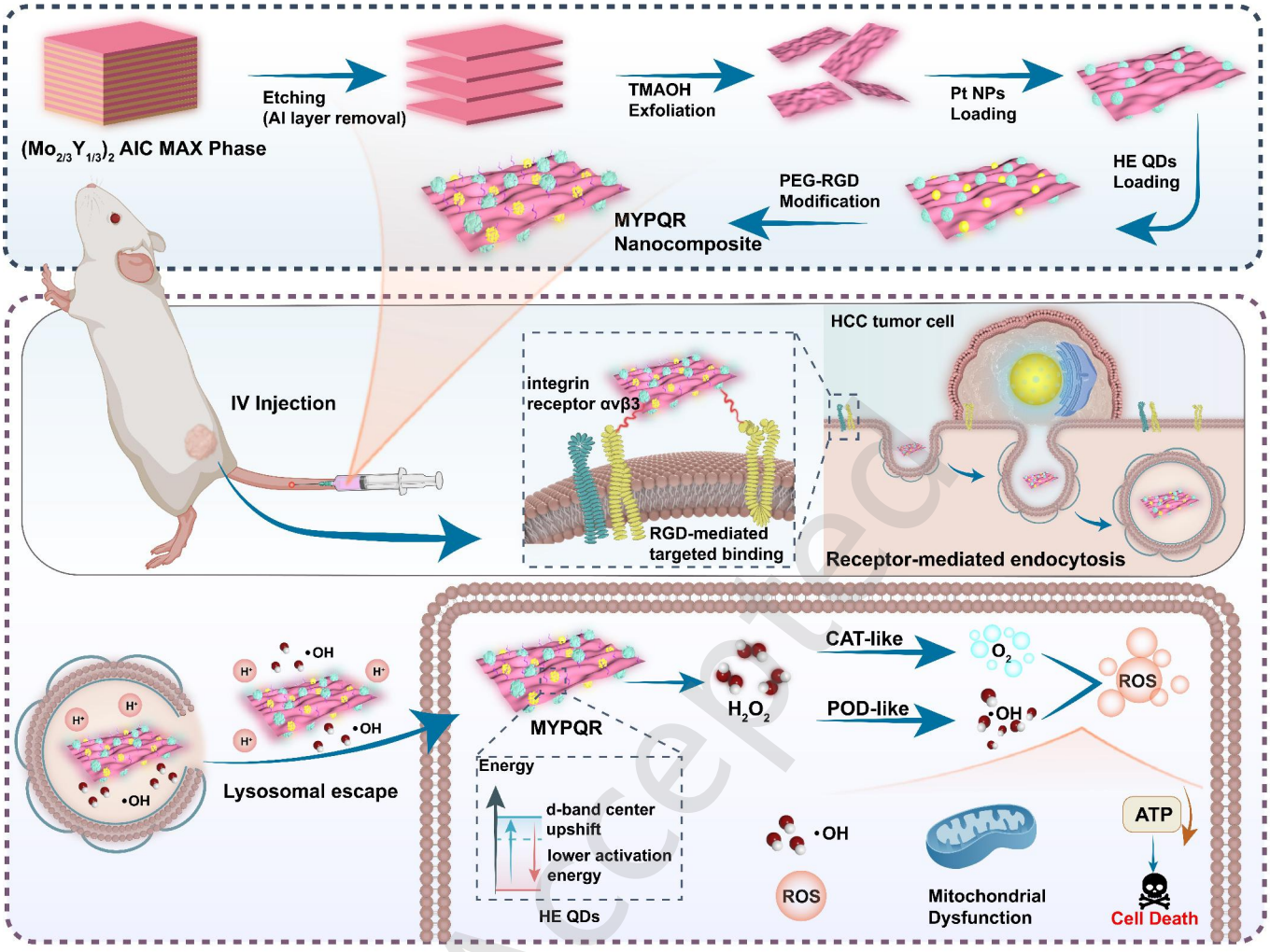
Nano Res., **Just Accepted Manuscript** • https://doi.org/10.26599/NR.2026.94909208

https://www.sciopen.com/journal/1998-0124 on Sep. 21, 2026

© The Authors(s)

Just Accepted

This is a "Just Accepted" manuscript, which has been examined by the peer-review process and has been accepted for publication. A "Just Accepted" manuscript is published online shortly after its acceptance,which is prior to technical editing and formatting and author proofing. Tsinghua University Press (TUP) provides "Just Accepted" as an optional and free service which allows authors to make their results available to the research community as soon as possible after acceptance. After a manuscript has been technically edited and formatted, and the page proofs have been corrected, it will be removed from the "Just Accepted" web site and published officially with volume and article number (e.g., *Nano Research*, **2025**, *18*, 94906990). Please note that technical editing may introduce minor changes to the manuscript text and/or graphics which may affect the content, and all legal disclaimers that apply to the journal pertain. In no event shall TUP be held responsible for errors or consequences arising from the use of any information contained in these "Just Accepted" manuscripts. To cite this anuscript please use its Digital Object Identifier (DOI®),which is identical for all formats of publication.



This work presents an RGD-modified $(Mo_{2/3}Y_{1/3})_2C$ MXene-based heterojunction nanozyme decorated with platinum nanoparticles and high-entropy $TiVNbMoC_3$ quantum dots. The nanoplatform modulates the electronic structure of Pt through interfacial charge redistribution, thereby enhancing its peroxidase-like and catalase-like activities for targeted cascade catalytic therapy of hepatocellular carcinoma. The nanocomposite effectively induces oxidative stress, mitochondrial dysfunction, and metabolic reprogramming in tumor cells, achieving potent antitumor efficacy with favorable biocompatibility in both cellular and xenograft mouse models.

Just Accepted

Nano Research

Open Access

Review Article/Research Article Please choose on

High-entropy quantum dots-modulated Pt/MXene heterojunction nanozymes for targeted catalytic therapy of hepatocellular carcinoma

Xiaodong Xu[1,§], Xiancheng Liu[2,§], Weiwei Shao[3], Yong Qiang[4], and Feiran Wang [5] ✉

[1] *Department of General Surgery, The First People's Hospital of Yancheng, Yancheng 224000, China*
[2] *Department of Radiation Oncology, Affiliated Hospital of Nantong University, Nantong 226000, China*
[3] *Department of Hepatobiliary Surgery, Beijing Chao-Yang Hospital affiliated to Capital Medical University, Beijing 100023, China*
[4] *Department of Hepatobiliary Surgery, JingMen People's Hospital, Jingchu University of Technology Affiliated JingMen People's Hospital, JingMen 448000, China*
[5] *Department of General Surgery, Affiliated Hospital of Nantong University, Nantong 226000, China*
[§] *Xiaodong Xu and Xiancheng Liu contributed equally to this work.*

Received: 15 July 2026; **Revised:** 17 September 2026; **Accepted:** 21 September 2026

✉ Address correspondence to wangfeirangs@ntu.edu.cn

Cite this article: *Nano Research*, 2026, 19, 94909208 https://doi.org/10.26599/NR.2026.94909208

ABSTRACT: Hepatocellular carcinoma (HCC) ranks among the most common and deadly malignancies worldwide; however, clinical management remains severely limited by the lack of effective therapeutic options. Although nanocatalytic therapy represents a targeted therapeutic strategy, its efficacy is often restricted by the complex tumor microenvironment. By decorating platinum (Pt) nanoparticles and high-entropy $TiVNbMoC_3$ quantum dots (HE QDs) onto $(Mo_{2/3}Y_{1/3})_2C$ nanosheets, followed by surface modification with RGD peptides, a targeted cascade nanocatalytic platform is constructed. Pt nanoparticles serve as the primary catalytic centers for enzyme-mimicking reactions, whereas HE QDs function as electronic modulators that form strong heterojunctions with Pt nanoparticles. This structure induces substantial interfacial charge redistribution and an upward shift in the Pt d-band center, thereby significantly reducing the activation energy. Upon cellular internalization, the platform exhibits peroxidase-like (POD-like) and catalase-like (CAT-like) activities, generating reactive oxygen species (ROS) and oxygen. *In vitro* and *in vivo* experiments demonstrate that the nanocomposite accumulates in tumor tissues, induces oxidative stress, and triggers metabolic reprogramming, as evidenced by mitochondrial dysfunction and reduced ATP production. This synergistic strategy effectively suppresses tumor growth, exhibits good biocompatibility, and provides a rational design approach for multifunctional nanotherapeutics.

KEYWORDS: hepatocellular carcinoma, nanozyme, high-entropy quantum dots, cascade catalytic therapy, metabolic reprogramming

Just Accepted

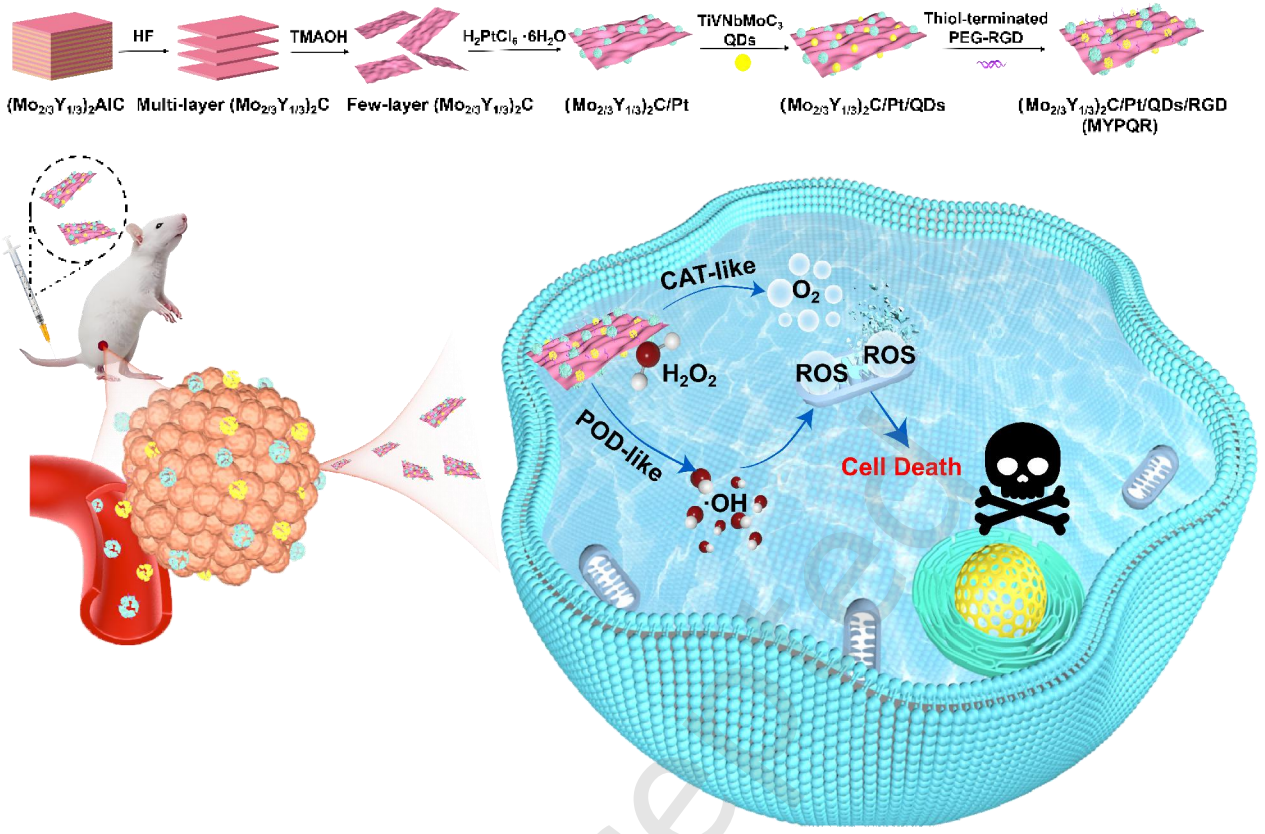
1 Introduction

As one of the most fatal malignancies worldwide, hepatocellular carcinoma (HCC) is characterized by consistently high mortality, and patients with advanced-stage disease exhibit a five-year survival rate below 20% [1-4]. Although conventional therapeutic approaches, including surgical resection, radiotherapy, and chemotherapy, have achieved substantial clinical progress, their efficacy in HCC remains frequently limited by high tumor heterogeneity, postoperative recurrence, and systemic adverse effects [5-9]. Recently, nanocatalytic therapy has emerged as a promising therapeutic strategy that exploits the tumor microenvironment (TME) to convert endogenous substrates, such as hydrogen peroxide (H_2O_2), into cytotoxic reactive oxygen species (ROS) in situ [10-13]. This approach offers improved therapeutic precision and reduced off-target toxicity compared with conventional chemotherapy. However, the complex characteristics of the TME, particularly the insufficient concentration of endogenous H_2O_2, often restrict the catalytic kinetics of nanomaterials, thereby limiting ROS generation and compromising effective tumor elimination [14-16].

To overcome these microenvironmental limitations, various nanocatalytic platforms, including metal–organic frameworks, single-atom catalysts, and bimetallic alloys, have been extensively investigated to enhance ROS generation [17-20]. Among these strategies, the integration of Pt nanoparticles with two-dimensional transition metal carbides (MXenes) has garnered substantial interest. In conventional Pt/MXene systems, commonly used MXenes (such as $Ti_3C_2T_x$) provide large specific surface areas and excellent electrical conductivity, whereas Pt nanoparticles exhibit dual enzyme-mimicking activities, including peroxidase-like (POD-like) and catalase-like (CAT-like) activities, enabling simultaneous hypoxia alleviation and oxidative stress induction [21-23]. Despite these advantages, current Pt/MXene-based catalysts still face several challenges. First, traditional Ti_3C_2 MXenes are susceptible to oxidation and structural degradation under complex physiological conditions, which may compromise their long-term stability and catalytic performance [24-26]. Second, from a physicochemical perspective, the intrinsic scaling relationships of Pt catalytic sites restrict the optimization of intermediate adsorption and desorption processes. Conventional single- or bimetallic promoters remain insufficient for precise regulation of Pt active sites, limiting further improvements in catalytic efficiency. Meanwhile, from a biological perspective, tumor cells exhibit substantial metabolic adaptability and can enhance antioxidant defense systems (e.g., glutathione, GSH) to counteract moderate oxidative stress [27-30]. Therefore, developing advanced nanocatalytic systems capable of precisely regulating interfacial electronic structures to maximize catalytic activity while simultaneously disrupting tumor energy metabolism remains highly desirable.

This study engineered a cascade nanocatalytic platform by integrating Pt nanoparticles and high-entropy $TiVNbMoC_3$ quantum dots onto a customized bimetallic $(Mo_{2/3}Y_{1/3})_2C$ MXene, followed by RGD peptide modification (denoted as MYPQR) (Scheme 1). This rational design addresses the aforementioned challenges from two perspectives. First, instead of conventional Ti_3C_2, the bimetallic $(Mo_{2/3}Y_{1/3})_2C$ MXene was selected as the substrate. The incorporation of Mo provides abundant variable-valence states to facilitate continuous redox reactions, whereas Y contributes to lattice stabilization, endowing the platform with enhanced physiological stability and synergistic electrochemical activity. Second, to overcome the catalytic limitations of Pt, ultra-small HE QDs were introduced as electronic modulators. Unlike traditional single-metal modifiers, high-entropy $TiVNbMoC_3$ QDs possess diverse d-orbital configurations that enable flexible regulation of Pt active sites. Specifically, robust heterojunctions formed between HE QDs and Pt trigger pronounced interfacial charge redistribution, thereby shifting the Pt d-band center upward. This electronic modulation alters conventional scaling relationships and reduces the activation energy of enzyme-mimicking reactions. At the cellular level, the MYPQR nanocomposite exhibits enhanced dual enzyme-mimicking activities, alleviating hypoxia through O_2 generation and inducing ROS-mediated apoptosis. Furthermore, the resulting oxidative stress promotes metabolic reprogramming, accompanied by mitochondrial dysfunction, ATP depletion, and glycolytic suppression. This study provides a strategy for enhanced targeted cancer therapy through the integration of high-entropy-driven interfacial electronic modulation and metabolic intervention.

Just Accepted



Scheme 1. Application of the $(Mo_{2/3}Y_{1/3})_2C$/Pt/QDs/RGD nanocomposite for enhanced cascade catalytic tumor therapy.

2 Experimental

2.1 Materials and Reagents

The MAX phase precursors, $(Mo_{2/3}Y_{1/3})_2AlC$ MAX and $TiVNbMoAlC_3$ MAX, were purchased from Suzhou Beike Nano Co., Ltd. (Suzhou, China). Hydrofluoric acid (HF, CAS:7664-39-3) was obtained from Rhawn Chemical Technology Co., Ltd. Tetramethylammonium hydroxide (TMAOH, CAS: 75-59-2), polyvinylpyrrolidone (PVP, CAS: 9003-39-8), chloroplatinic acid hexahydrate ($H_2PtCl_6 \cdot 6H_2O$, CAS: 18497-13-7), and 3,3′,5,5′-tetramethylbenzidine (TMB, CAS: 54827-17-7) were supplied by Aladdin Biochemical Technology Co., Ltd. (Shanghai, China). GSH (Cat.No. HY-D0187), RGD (Cat.No. HY-P1740) peptides and HIF-α (Cat.No. HY-P80704) were procured from MedChemExpress (MCE). The $[Ru(dpp)_3]Cl_2$ (CAS: 36309-88-3) fluorescent probe was obtained from Shanghai Maokang Biotechnology Co., Ltd. DCFH-DA probe (Cat.No. S0035S), JC-1 dye (Cat.No. C2003S), Mito-Tracker Green (Cat.No. C1048) and Lyso-Tracker Green (Cat.No. C1047S) were procured from Beyotime Biotechnology Co., Ltd. (Shanghai, China). The human HCC cell line HCC-LM3 was acquired from Shanghai Fuheng Biotechnology Co., Ltd. Five-week-old SPF-grade nude mice were procured from Speford (Suzhou) Biotechnology Co., Ltd.

2.2 Synthesis of Monolayer $(Mo_{2/3}Y_{1/3})_2C$ MXene Nanosheets

Briefly, 1 g of $(Mo_{2/3}Y_{1/3})_2AlC$ MAX phase powder was thoroughly mixed with 20 mL of deionized water and subsequently immersed in a 48 wt% HF solution. Using a magnetic stirrer, the mixture underwent continuous stirring at room temperature for 12 h to selectively remove the aluminum layer. After the reaction, the mixture underwent centrifugation at 4000 rpm for 5 min in centrifuge tubes. The supernatant was then discarded, and the remaining solid was redispersed in deionized water using ultrasonication. This procedure was repeated iteratively until the pH of the supernatant reached a stable value between 6 and 7. The resulting precipitate was collected and freeze-dried for 24 h to obtain multilayer $(Mo_{2/3}Y_{1/3})_2C$ MXene. The as-prepared product was subsequently intercalated and exfoliated using a 5 wt% TMAOH aqueous solution under magnetic stirring at 500–600 rpm and 55°C for 4 h. After being transferred into centrifuge tubes, the resulting suspension underwent centrifugation at 10,000 rpm for 5–10 min. The precipitate was removed, and the supernatant was washed five times with 250 mL of deionized water through repeated centrifugation until the pH reached approximately 6. Finally, the stable dark supernatant containing single-layer $(Mo_{2/3}Y_{1/3})_2C$ MXene nanosheets was collected

Just Accepted

and freeze-dried for 48 h.

2.3 Synthesis of High-Entropy $TiVNbMoC_3$ Quantum Dots

Briefly, 5 g of $TiVNbMoAlC_3$ MAX phase powder was slowly added to a polyethylene reaction vessel containing 50 mL of 48 wt% HF solution. Selective etching of the aluminum layer was performed at 55°C under magnetic stirring at 400 rpm for 96 h. After centrifuging at 4000 rpm for 5 min, deionized water was used to wash the mixture repeatedly until the pH value of the resulting supernatant stabilized at 6–7. The precipitate was collected and dispersed in a 5 wt% TMAOH aqueous solution. Exfoliation was conducted under magnetic stirring at 500–600 rpm and 55°C for 4 h. The resulting suspension underwent centrifugation at 10,000 rpm for 5 min, followed by five washes with approximately 250 mL of deionized water via repeated centrifugation until reaching a pH of approximately 6. The stable supernatant containing single-layer high-entropy MXene was collected and freeze-dried for 24 h. High-entropy quantum dots were prepared by dispersing 100 mg of the obtained high-entropy MXene in 20 mL of deionized water, followed by sonication until a uniform suspension was obtained. After the addition of 20 mg of GSH, the mixture was further sonicated for 5 min. After being transferred to a polytetrafluoroethylene-lined autoclave, the mixture underwent 10 min of high-power microwave irradiation, producing high-entropy $TiVNbMoC_3$ quantum dots ($TiVNbMoC_3$ QDs).

2.4 Synthesis of the $(Mo_{2/3}Y_{1/3})_2C$/Pt Composite

$H_2PtCl_6 \cdot 6H_2O$ (50.80 mg) was ultrasonically dispersed in 20 mL of ethylene glycol containing 222 mg of PVP. The mixture was transferred into a three-necked flask and heated to 180°C under magnetic stirring for 10 min, followed by natural cooling to ambient conditions to obtain a dark brown solution. The resulting product was centrifuged and washed three times with acetone to collect the Pt nanoparticles. The nanoparticles were then redispersed in 10 mL of deionized water. Separately, 10 mL of $(Mo_{2/3}Y_{1/3})_2C$ MXene suspension was diluted with 50 mL of deionized water. Under vigorous magnetic stirring, the prepared Pt nanoparticle suspension was slowly added dropwise to the $(Mo_{2/3}Y_{1/3})_2C$ MXene dispersion. The mixture was continuously stirred at ambient conditions for 8 h. After collection by centrifugation, the product was rinsed with deionized water and subsequently freeze-dried, producing the $(Mo_{2/3}Y_{1/3})_2C$/Pt composite material.

2.5 Synthesis of the $(Mo_{2/3}Y_{1/3})_2C$/Pt/QDs Composite

Briefly, 20 mg of the $(Mo_{2/3}Y_{1/3})_2C$/Pt composite material was suspended in 10 mL deionized water via sonication for 5 min until a uniform suspension formed. Subsequently, 2 mL of the synthesized $TiVNbMoC_3$ quantum dot solution (1 mg/mL) was introduced into the suspension, followed by further ultrasonication for 5 min. The mixture was then magnetically stirred at ambient conditions for 6 h to facilitate the adsorption of QDs onto the MXene surface. Finally, the product was rinsed with deionized water, separated by centrifugation (8000 rpm, 5 min), and dried in a vacuum oven at 60°C for 12 h. The resulting $(Mo_{2/3}Y_{1/3})_2C$/Pt/QDs composite material was collected for further use.

2.6 Synthesis and Preparation of RGD-Functionalized Composite Nanosheets

To synthesize the three RGD-modified materials, suspensions of $(Mo_{2/3}Y_{1/3})_2C$, $(Mo_{2/3}Y_{1/3})_2C$/Pt, and $(Mo_{2/3}Y_{1/3})_2C$/Pt/QDs composite nanosheets were individually added dropwise to RGD solutions. Each mixture was subjected to ultrasonic oscillation for 30 min and subsequently incubated at ambient conditions for 60 min. The suspensions subsequently underwent centrifugation at 16,000 rpm for 30 min. After discarding the supernatants, the pellets obtained underwent resuspension in a suitable solvent, yielding $(Mo_{2/3}Y_{1/3})_2C$/RGD, $(Mo_{2/3}Y_{1/3})_2C$/Pt/RGD, and $(Mo_{2/3}Y_{1/3})_2C$/Pt/QDs/RGD suspensions. For clarity, $(Mo_{2/3}Y_{1/3})_2C$/RGD, $(Mo_{2/3}Y_{1/3})_2C$/Pt/RGD, and $(Mo_{2/3}Y_{1/3})_2C$/Pt/QDs/RGD are abbreviated as MoY-C, MoY-C/Pt, and MYPQR, respectively, hereafter.

2.7 Density Functional Theory Calculation

Structural relaxation and electronic properties of the constructed models were investigated through first-principles calculations based on density functional theory (DFT), implemented via the CASTEP module in the Materials Studio software package. The generalized gradient approximation (GGA) with the Perdew–Burke–Ernzerhof (PBE) functional was adopted to describe exchange-correlation effects. On-the-fly generated (OTFG) ultrasoft pseudopotentials were used to represent interactions between ionic cores and valence electrons. A plane-wave cutoff energy of 600 eV was set, and a Monkhorst–Pack k-point grid of 1 × 2 × 1 was applied for Brillouin zone sampling. During geometric optimization, the convergence criteria were set as follows: energy change per atom < 1.0×10^{-5} eV,

Just Accepted

maximum force < 0.03 eV/Å, maximum displacement < 1.0×10^{-3} Å, and self-consistent field (SCF) energy convergence threshold of 1.0×10^{-6} eV.

2.8 Quantification of POD Enzyme Activity

POD-like activity was assessed with TMB as substrate. To prepare the NaAc buffer, 450 mg NaAc was dissolved in 25 mL deionized water, and pH was subsequently adjusted to 3–4 with 0.5 mL acetic acid. TMB (5 mM) and H_2O_2 (1%) solutions were also prepared. The reaction mixture consisted of 800 μL of NaAc buffer, 100 μL of TMB solution, and 150 μL of $(Mo_{2/3}Y_{1/3})_2C$, $(Mo_{2/3}Y_{1/3})_2C$/Pt, or $(Mo_{2/3}Y_{1/3})_2C$/Pt/QDs suspension (200 μg/mL). Prior to initiating the assay, the material suspension was thoroughly vortex-mixed to ensure uniform nanocomposite dispersion. Subsequently, the reaction was initiated by adding 200 μL of H_2O_2 solution. After the reaction, the characteristic absorption peak at 650 nm was recorded for quantitative analysis of POD-like activity.

2.9 Measurement of CAT Enzyme Activity

CAT-like enzyme activity was assessed using the $[Ru(dpp)_3]Cl_2$ oxygen indicator probe. A reaction mixture was prepared by combining 100 μM H_2O_2 and varying concentrations of $(Mo_{2/3}Y_{1/3})_2C$/Pt/QDs in 0.1 M Tris-HCl buffer. Prior to each measurement, the reaction mixture was thoroughly vortexed to ensure complete and uniform suspension of the nanoparticles, followed immediately by fluorescence detection at 450 nm after adding 10 μL of $[Ru(dpp)_3]Cl_2$ solution in DMSO (10 mg/mL).

Additionally, a portable dissolved oxygen meter was used to directly monitor oxygen generation. Briefly, 10 μL of 30% H_2O_2 solution was combined with 15 mL of deionized water, after which 2 mL of material suspension (100 μg/mL) was introduced. To maintain homogenous dispersion, the suspension was vortex-mixed thoroughly before immediate recording. The generated dissolved oxygen concentration was recorded continuously from 0 to 5 min (unit: mg/L). The catalytic kinetics of H_2O_2 decomposition by the three materials were determined under identical mixing conditions upon adding the H_2O_2 solution to the buffer system.

2.10 Cell Culture

The human hepatocellular carcinoma cell line (HCC-LM3) and human umbilical vein endothelial cell line (HUVEC) were cultured in Dulbecco's Modified Eagle's Medium (DMEM). The human normal hepatocyte cell line (LO2) was maintained in RPMI-1640 medium. All media were supplemented with 10% fetal bovine serum (FBS) and 1% penicillin-streptomycin. All cell lines (HCC-LM3, L02, and HUVEC) within passages 3 to 10 (P3 – P10) were used for all experiments, and all cellular assays were performed with cells harvested during the logarithmic growth phase. All cells were incubated at 37℃ in a humidified atmosphere containing 5% CO_2.

2.11 CCK-8 Assay for Cell Viability

HCC-LM3 cells, LO2 cells, and HUVEC cells were seeded into 96-well plates and cultured until reaching approximately 40% confluence. Cells subsequently underwent treatment with varying concentrations (5, 10, 20, 50, and 100 μg/mL) of MoY-C, MoY-C/Pt, and MYPQR for 24 h. After treatment, 10 μL of CCK-8 solution was introduced into each well, and plates were incubated for an additional 2 h at 37°C under a humidified 5% CO_2 atmosphere. Cell viability was determined by measuring absorbance at 450 nm with a microplate reader.

2.12 Transwell Assay

HCC-LM3 cells were maintained in serum-free medium for 24 h before receiving treatment with 1 μg/mL MoY-C, MoY-C/Pt, or MYPQR. The cells were then resuspended and seeded into Transwell chambers alongside the respective samples. After incubating for 24 and 48 h at 37℃ under 5% CO_2, non-migrated cells on the upper membrane were eliminated, and migrated cells underwent 30-min fixation in 4% paraformaldehyde (PFA), 10-min staining with crystal violet, PBS washing, and subsequent microscopic imaging.

2.13 Wound Healing Assay

HCC-LM3 cells were placed into six-well plates and grown until reaching 80% confluence. After overnight incubation, cells underwent treatment with 1 μg/mL of MoY-C, MoY-C/Pt, and MYPQR for 48 h. The medium was then replaced with serum-free medium, and cells were maintained for an additional 6 h. A scratch was introduced into the cell monolayer, and the initial scratch width was recorded by photographing the cells. Cells were subsequently maintained in serum-free medium for 24 and 48 h, and the scratch width was photographed at each time point. The effect of different materials on cell migration was evaluated by comparing the scratch widths at the initial and subsequent time points using the photographs.

Just Accepted

2.14 Hemolysis Assay

Murine blood samples collected from 6-week-old C57 mice were defibrinated and washed with 0.9% saline to prepare a 4% red blood cell (RBC) suspension. The RBC suspension was then incubated with MoY-C, MoY-C/Pt, or MYPQR at concentrations ranging from 5 to 200 μg/mL for 1 h at 37°C. Following centrifugation at 1000 × g for 3 min, hemolysis was evaluated based on the color of the supernatant.

2.15 Cellular Uptake and Receptor-Targeting Assays

HCC-LM3 cells were seeded into confocal dishes and incubated with 5 μg/mL Cy5.5-labeled MYPQR (Cy5.5-MYPQR) for 3, 6, and 12 h. To evaluate RGD-mediated targeting specificity, two control groups were established: one group was treated with non-RGD-functionalized Cy5.5-$(Mo_{2/3}Y_{1/3})_2C$/Pt/QDs, while another group was pretreated with excess free RGD peptide before incubation with Cy5.5-MYPQR for competitive inhibition. After treatment, the cells were washed with PBS and stained with DiO to label cytoplasmic membranes (37℃, 30 min), followed by DAPI staining for nuclear labeling. The intracellular distribution of the fluorescent nanocomposites was visualized using CLSM.

2.16 DCFH-DA Reactive Oxygen Species Detection

HCC-LM3 cells were seeded into confocal dishes and exposed to 5 μg/mL MoY-C, MoY-C/Pt, or MYPQR for 24 h. Subsequently, cells were rinsed with PBS and underwent incubation with CM-H_2DCFDA (diluted to 5 μM at a 1:1000 ratio) at 37°C for 30 min. After incubation,cells were rinsed three times with serum-free medium to eliminate residual probe. Intracellular ROS generation was subsequently observed using a fluorescence microscope, with green fluorescence (Ex/Em = 495/530 nm) indicating ROS levels.

2.17 Immunofluorescence Staining for HIF-1α Expression

HCC-LM3 cells were seeded into confocal dishes and exposed to 5 μg/mL MoY-C, MoY-C/Pt, or MYPQR for 24 h in the presence of $CoCl_2$ (150 μM, 24 h) to induce chemical hypoxia. Samples were then fixed with 4% paraformaldehyde for 15 min, permeabilized with 0.2% Triton X-100 for 10 min, and blocked with 5% BSA for 1 h at room temperature. Subsequently, the samples were incubated with anti-HIF-1α primary antibody (1:200) at 4℃ overnight. After washing three times with PBS, the samples were incubated with the corresponding fluorophore-conjugated secondary antibody for 1 h in the dark at room temperature, followed by DAPI counterstaining for 5 min to label cell nuclei. Finally, fluorescence images were acquired using CLSM to quantify HIF-1α expression levels and nuclear translocation.

2.18 JC-1 Mitochondrial Membrane Potential Detection

Cells at approximately 80% confluence were treated with 5 μg/mL MoY-C, MoY-C/Pt, or MYPQR for 24 h. After a 4 h recovery in complete medium, cells underwent incubation with JC-1 dye at 37°C for 30 min, were rinsed with JC-1 buffer, and subsequently counterstained with Hoechst. Fluorescence images were captured by CLSM, with JC-1 monomers visualized at Ex/Em = 490/530 nm and JC-1 aggregates visualized at Ex/Em = 525/590 nm.

2.19 Mitochondrial Targeting and Lysosomal Escape Assays

HCC-LM3 cells were seeded into confocal dishes and cultured overnight. After replacing the culture medium, the cells were incubated with Cy5.5-MYPQR for various time intervals (2, 4, and 8 h) and then washed with PBS. Subsequently, Mito-Tracker Green (100 nM, 30 min) or Lyso-Tracker Green (75 nM, 30 min) was added to specifically label the mitochondria or lysosomes, respectively. After washing, the cells were directly observed using CLSM to evaluate the red/green fluorescence co-localization and separation.

2.20 *In Vivo* Antitumor Activity

To perform in vivo experiments, 5-week-old female BALB/c nude mice were maintained in a specific pathogen-free (SPF) barrier facility under strictly controlled conditions (12 h light/12 h dark cycle, 22 ± 2℃, 50 ± 10% relative humidity) with ad libitum access to sterile food and water and biweekly aseptic cage/corn cob bedding changes; all animal protocols were approved by the Animal Ethics Committee of Nantong University (IACUC20230721-002). For optical fluorescence imaging, mice bearing subcutaneously xenografted HCC-LM3 tumors (5 × 10^6 cells/mL in the right axillary region, volume reached 100 mm^3) were intravenously injected via tail vein with Cy5.5-$(Mo_{2/3}Y_{1/3})_2C$/Pt/QDs or Cy5.5-MYPQR (5 mg/kg, 200 μL), anesthetized with isoflurane for in vivo optical imaging at designated time intervals (1, 6, 12, 24, and 36 h), and subsequently euthanized at 36 h post-injection to harvest major

Just Accepted

organs and tumors for ex vivo fluorescence imaging and average radiance region-of-interest (ROI) quantification. For in vivo anti-tumor efficacy and biosafety evaluation, HCC-LM3 xenograft models (5×10^6 cells/mL) were randomly assigned to four groups (n = 5 per group)—PBS, MoY-C, MoY-C/Pt, and MYPQR—and administered intravenous treatments at 5 mg/kg (200 μL per injection) every other day for 14 days while tumor growth was monitored using a vernier caliper ($V = 1/2 \times a \times b^2$, where a and b represent long and short diameters, respectively). Upon completion of the 14-day therapeutic regimen, whole blood and serum were collected for routine hematological (WBC, RBC, HGB, PLT) and blood biochemical (ALT, AST, BUN, CREA) assays to evaluate systemic, hepatic, and renal toxicity, after which mice were euthanized and excised tumors were weighed and fixed in 4% PFA for histological assessments, including H&E staining, TUNEL apoptosis assays (using TdT reaction buffer and DAPI counterstaining), and Ki67 immunofluorescence staining (1:1000 dilution) visualized via light or confocal microscopy.

2.21 MALDI-TOF Mass Spectrometry Analysis

Tumor tissues collected from mice after treatment with PBS, MoY-C, MoY-C/Pt, and MYPQR were prepared into frozen sections and submitted to the Shandong Provincial Analysis and Testing Center for comprehensive metabolomic analysis.

2.22 Statistical Analysis

Normality tests were performed on all experimental data prior to statistical analysis.

All quantitative data are denoted as mean ± standard deviation and displayed with error bars in the figures. Each experiment was statistically analyzed with a sample size of n = 3, as indicated in the corresponding figure legends. One-way analysis of variance (ANOVA), followed by Tukey's post hoc test, was applied to determine statistical differences among multiple groups. Statistical significance was defined as follows: *P < 0.05, **P < 0.01, ***P < 0.001, and ****P < 0.0001. GraphPad Prism version 10.1.2 and Origin 2022 software were used for all statistical analyses.

3 Results and discussion

3.1 Synthesis and Morphology Characterization

To construct this multifunctional nanotheranostic platform, a "top-down" etching strategy combined with a "bottom-up" self-assembly approach was employed to prepare $(Mo_{2/3}Y_{1/3})_2C$/Pt/QDs. First, selective etching of the MAX phase precursor $(Mo_{2/3}Y_{1/3})_2AlC$ was performed. The SEM image clearly reveals the typical accordion-like multilayered structure, consistent with previously reported morphologies [31, 32], indicating the successful removal of the Al layer (Fig. 1a). Subsequently, after TMAOH intercalation and ultrasonication-assisted exfoliation, the TEM image confirms the transformation of the material into transparent, ultrathin monolayer $(Mo_{2/3}Y_{1/3})_2C$ two-dimensional nanosheets with an average lateral dimension of approximately 150 - 200 nm (Fig. 1b). These nanosheets exhibit smooth surfaces without apparent defects, providing an ideal substrate with a large specific surface area for the loading of additional components.

To introduce the high-entropy effect for regulating catalytic active sites, $TiVNbMoC_3$ QDs were synthesized and decorated onto the $(Mo_{2/3}Y_{1/3})_2C$ nanosheets. The TEM image demonstrates that the prepared QDs exhibit excellent monodispersity and spherical morphology, with a uniform size distribution centered at approximately 2 - 5 nm in diameter (Fig. 1c). Atomic force microscopy (AFM) was further employed to characterize the three-dimensional morphology and height distribution of the QDs, confirming their ultra-small nanoscale dimensions, with heights mainly distributed below 3 nm (Fig. S1). This extremely small size facilitates high-density loading onto the carrier surface and maximizes the exposure of active sites [33-35].

Subsequently, Pt nanoparticles and high-entropy QDs were co-assembled onto the surface of the MXene nanosheets. The TEM image of the composite material clearly shows that abundant QDs and Pt nanoparticles are uniformly anchored on the two-dimensional nanosheet surface, which largely retains its lateral dimension of approximately 200 nm, without obvious aggregation (Fig. 1d). The formation of intimate heterointerfaces between these components is observed. Furthermore, energy-dispersive X-ray spectroscopy (EDS) elemental mapping confirmed the uniform distribution of five high-entropy component elements (Mo, V, Nb, Y, and Ti) together with Pt on the nanosheet surface, directly demonstrating the successful incorporation of high-entropy components (Fig. 1e and Fig. S2). AFM was further conducted to quantitatively assess the topographical features and thickness of the exfoliated

Just Accepted

$(Mo_{2/3}Y_{1/3})_2C$ nanosheets (Fig. 1f). The corresponding height profile reveals a uniform thickness of approximately 6.0 nm, confirming the successfully delaminated monolayer structure of the $(Mo_{2/3}Y_{1/3})_2C$ MXene nanosheets (Fig. 1g).

Finally, to evaluate the dispersion behavior of the nanocomposite in aqueous solution, the hydrodynamic size and surface charge of pristine MXene nanosheets were compared with those of the loaded $(Mo_{2/3}Y_{1/3})_2C$/Pt/QDs nanocomposite. Dynamic light scattering (DLS) and zeta potential measurements demonstrated that, despite the incorporation of substantial amounts of metal nanoparticles and quantum dots, the $(Mo_{2/3}Y_{1/3})_2C$/Pt/QDs nanocomposite maintained a relatively uniform hydrodynamic size distribution, with a peak value of approximately 210 - 220 nm, and exhibited a stable negative surface potential of approximately -30 mV (Fig. 1h-i and Fig. S3). To evaluate its physiological stability, the $(Mo_{2/3}Y_{1/3})_2C$/Pt/QDs nanocomposite was incubated in PBS and 10% FBS for 48 h. Both the zeta potential (Fig. S4) and hydrodynamic size (Fig. S5) remained stable without noticeable aggregation, confirming excellent colloidal stability under physiological conditions.

To further elucidate the chemical interactions among functional components and their influence on material properties, X-ray photoelectron spectroscopy (XPS) and X-ray diffraction (XRD) analyses were conducted to characterize the nanocomposite's chemical composition, elemental valence states, and crystal structures. First, XRD patterns further confirmed the crystal structures and successful integration of the composite components (Fig. 1j). As shown in the XRD spectrum, pristine $(Mo_{2/3}Y_{1/3})_2C$ MXene exhibits a prominent and sharp diffraction peak at $2\theta \approx 7.5°$, corresponding to the (002) plane and confirming its typical two-dimensional layered structure. Additional characteristic MXene diffraction peaks are observed at approximately 27.5°, 36.0°, and 41.5°. For the high-entropy QDs, the diffraction pattern displays relatively broad features without distinct sharp peaks, consistent with their ultra-small nanoscale dimensions (2–5 nm). In the XRD pattern of the $(Mo_{2/3}Y_{1/3})_2C$/Pt/QDs composite, the characteristic layered structural peaks of the MXene substrate (e.g., at 7.5° and 27.5°) are well preserved. Meanwhile, diffraction peaks corresponding to the face-centered cubic (fcc) Pt nanoparticles, including the characteristic Pt (111) peak at approximately 39.8° and the (220) peak near 67.5°, are observed in the composite pattern. These results are consistent with the TEM observations, demonstrating that both ultra-small HE QDs and Pt nanoparticles were successfully anchored onto the intact MXene nanosheets.

XPS analysis was further performed to investigate the electronic states of the constituent elements. The survey spectrum confirmed the coexistence of Mo, Y, Ti, Nb, V, Pt, and C elements (Fig. 1k-l and Fig. S6). In the high-resolution spectra, Mo is mainly present in the Mo^{6+} state, which may serve as a catalytic active species, whereas V exhibits mixed valence states of V^{4+}/V^{5+}, suggesting its potential involvement in electron transfer during redox reactions. Ti (Ti^{4+}) and Y (Y^{4+}) primarily contribute to structural stabilization, while Nb exists predominantly in the Nb^{5+} state and provides favorable electronic characteristics. Notably, Pt is mainly present in the zero-valent state (Pt^0), which is essential for efficient POD-like and CAT-like catalytic activities. The C 1s spectrum exhibits characteristic signals corresponding to C–C, C–Mo/Ti bonds, and oxygen-containing functional groups, confirming the typical surface chemical features of MXene. Importantly, slight shifts in the binding energies of various elements compared with standard values provide evidence of electronic interactions among the high-entropy quantum dots, Pt nanoparticles, and MXene substrate. Such electronic structure modulation may contribute to the enhanced catalytic performance of the composite material. Furthermore, VB-XPS spectra were collected to determine the valence band maximum (VBM) edges and evaluate the energy level alignment. The valence band maximum relative to the Fermi level (E_{VB}) was determined to be 1.83 eV for $(Mo_{2/3}Y_{1/3})_2C$ nanosheets (Fig. 1m) and 2.41 eV for high-entropy QDs (Fig. 1n). These distinct Fermi-level-referenced electronic states establish a clear energy band offset between the MXene substrate and HE QDs. This energetic mismatch drives intrinsic interfacial charge redistribution, thereby modulating the electronic structure of Pt active sites across the heterojunction.

Just Accepted

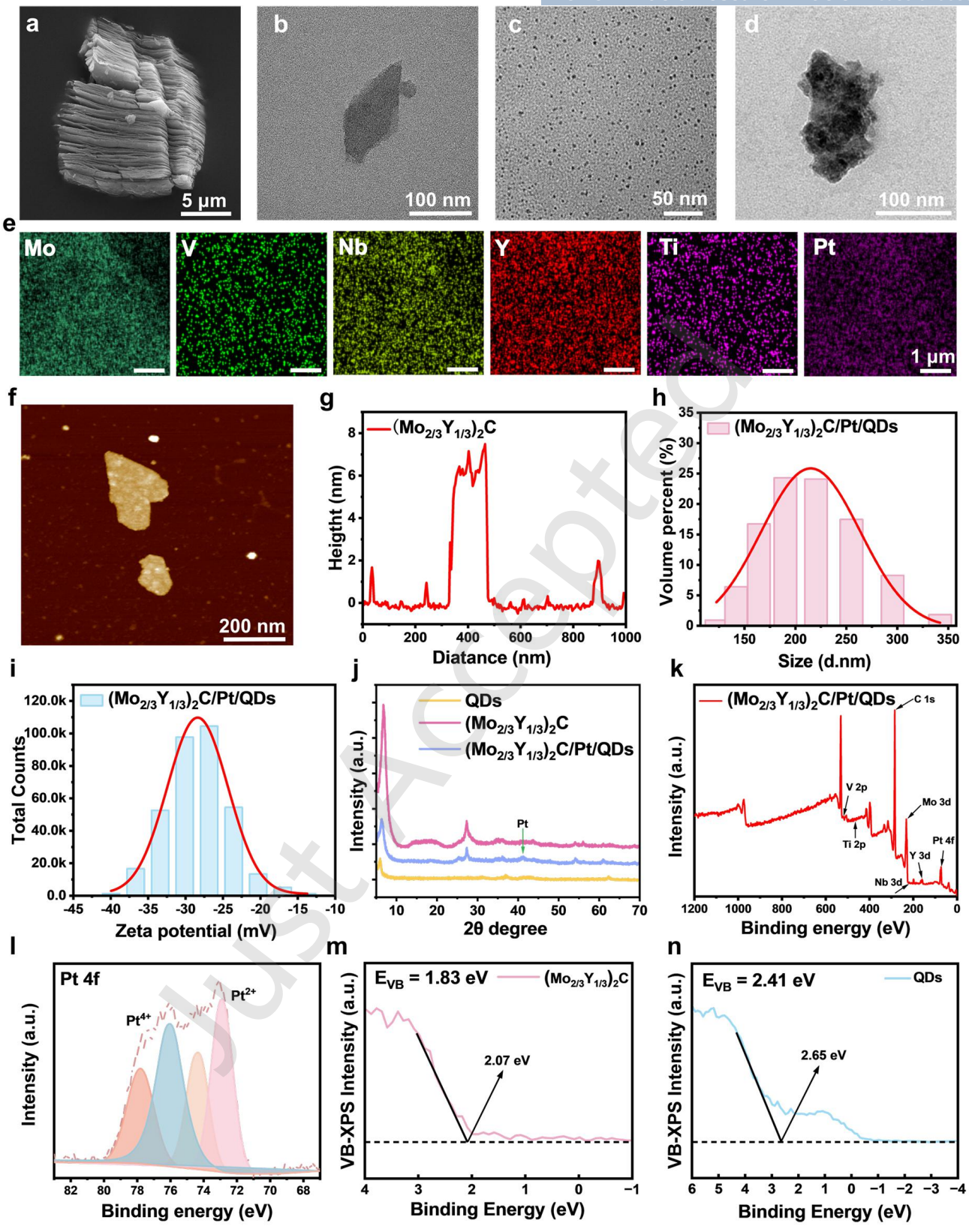


Figure 1. Characterization of the $(Mo_{2/3}Y_{1/3})_2C$/Pt/QDs nanocomposite. (a) SEM image of multi-layer $(Mo_{2/3}Y_{1/3})_2C$ nanosheets. TEM images of (b) Few-layer $(Mo_{2/3}Y_{1/3})_2C$ nanosheets, (c) high-entropy QDs, and (d) the $(Mo_{2/3}Y_{1/3})_2C$/Pt/QDs composite. (e) Corresponding elemental mapping images of the $(Mo_{2/3}Y_{1/3})_2C$/Pt/QDs composite. (f) AFM image of few-layer $(Mo_{2/3}Y_{1/3})_2C$ and (g) corresponding height distribution profile. (h) Hydrodynamic size distribution and (i) zeta potential distribution of the $(Mo_{2/3}Y_{1/3})_2C$/Pt/QDs composite. (j) XRD patterns of $(Mo_{2/3}Y_{1/3})_2C$ MXene, QDs, and the $(Mo_{2/3}Y_{1/3})_2C$/Pt/QDs composite. (k) Wide-scan XPS spectrum of the $(Mo_{2/3}Y_{1/3})_2C$/Pt/QDs composite. (l) High-resolution XPS spectrum of Pt 4f. VB-XPS spectra of (m)

Just Accepted

$(Mo_{2/3}Y_{1/3})_2C$ nanosheets and (n) HE QDs.

3.2 Density functional theory explanation of the catalytic enhancement mechanism

Previous studies have demonstrated that heterointerfaces can induce significant charge redistribution, orbital hybridization, and modulation of electronic properties. To elucidate the interaction mechanism between QDs and Pt in the $(Mo_{2/3}Y_{1/3})_2C$/Pt/QDs composite system, differential charge density distribution (Δρ), electronic band structure, and projected density of states (PDOS) were calculated (Fig. S7). As shown in Fig. 2a and Fig. S8, the interfacial charge transfer behavior was clearly visualized. Electron accumulation regions (red) were mainly localized on the QDs side, whereas electron depletion regions (blue) were primarily distributed around Pt atoms, indicating strong electronic interactions between Pt and QDs. Further analysis of the band structure and PDOS revealed that QD adsorption reduced the band gap of the system from 0.06 eV to 0.02 eV (Fig. 2b and Fig. S9). This result suggests that a lower energy barrier is required for electron transfer in the $(Mo_{2/3}Y_{1/3})_2C$/Pt/QDs system, thereby facilitating catalytic reactions. The PDOS results further revealed pronounced hybridization between the d-orbitals of QD elements, such as Mo and Ti, and the Pt d-orbitals, with the hybridized states shifting toward higher energy levels (Fig. 2c). Per d-band center theory, shifting the d-band center upward strengthens the adsorption of reaction intermediates, thereby enhancing catalytic activity. Theoretical calculations further indicated that the multi-element synergy within the HE QDs induces a prominent near-neighbor effect at the heterojunction interface. Specifically, extensive hybridization between the metal d-orbitals of QDs and Pt 5d orbitals facilitates interfacial charge transfer and contributes to band gap reduction. Importantly, this strong electronic interaction drives an upward shift of the Pt d-band center toward a more favorable position. Such electronic structure modulation optimizes the adsorption and desorption behavior of reactive intermediates (e.g., •OH and O_2), thereby modifying the conventional scaling relationships of Pt catalysts and improving the catalytic performance of the $(Mo_{2/3}Y_{1/3})_2C$/Pt/QDs nanocomposite.

To evaluate the enzyme-mimicking activities of the $(Mo_{2/3}Y_{1/3})_2C$/Pt/QDs nanocomposite, systematic characterization of its POD-like and CAT-like catalytic performances was performed. Electron spin resonance (ESR) spectroscopy was further employed to investigate ROS generation and elucidate the underlying catalytic mechanism [36, 37]. As shown in Fig. 2d, all experimental groups exhibited the characteristic 1:2:2:1 intensity pattern of DMPO–•OH adduct signals. Among them, the $(Mo_{2/3}Y_{1/3})_2C$/Pt/QDs group showed the strongest signal intensity, confirming its enhanced ability to generate hydroxyl radicals (•OH) in the presence of H_2O_2. In the TMB–H_2O_2 reaction system, $(Mo_{2/3}Y_{1/3})_2C$/Pt/QDs exhibited the highest catalytic oxidation activity [38]. Compared with pristine MXene and $(Mo_{2/3}Y_{1/3})_2C$/Pt, the $(Mo_{2/3}Y_{1/3})_2C$/Pt/QDs composite displayed significantly increased characteristic absorbance, accompanied by a clear concentration-dependent trend (Fig. 2e and Fig. S10).

In addition to POD-like activity, the nanocomposite exhibited excellent CAT-like activity. Dissolved oxygen monitoring experiments demonstrated that $(Mo_{2/3}Y_{1/3})_2C$/Pt/QDs efficiently catalyzed the decomposition of H_2O_2 to generate O_2. Within a reaction time of 300 s, the increase in dissolved oxygen concentration (ΔC) reached approximately 15.2 $mg \cdot L^{-1}$, showing superior oxygen generation performance compared with $(Mo_{2/3}Y_{1/3})_2C$/Pt (approximately 14.5 $mg \cdot L^{-1}$). This oxygen generation capacity exhibited a positive correlation with material concentration (Fig. 2f and Fig. S11). The generation of O_2 was further quantitatively confirmed using the $[Ru(dpp)_3]Cl_2$ oxygen-sensitive probe, whose fluorescence intensity is dynamically quenched by oxygen (Fig. 2g). To quantitatively evaluate the synergistic enhancement effect of HE QDs on the enzymatic activity of Pt, steady-state kinetic parameters were calculated based on the Michaelis–Menten equation (Fig. 2h-i). Radar chart analysis revealed that the POD-like maximum reaction rate (V_{max}) of $(Mo_{2/3}Y_{1/3})_2C$/Pt/QDs reached approximately 0.19 $\mu M \cdot min^{-1}$, representing an approximately 46% increase compared with the $(Mo_{2/3}Y_{1/3})_2C$/Pt group (0.13 $\mu M \cdot min^{-1}$). Similarly, the CAT-like reaction V_{max} increased from 2.8 $\mu M \cdot min^{-1}$ to 3.8 $\mu M \cdot min^{-1}$, corresponding to an enhancement of approximately 35%. In summary, as illustrated in Fig. 2j, the introduction of QDs effectively modulated the electronic structure and catalytic activity of the active sites, endowing $(Mo_{2/3}Y_{1/3})_2C$/Pt/QDs with enhanced dual enzyme-mimicking activities. These properties enabled simultaneous ROS generation and hypoxia alleviation within the TME, providing a foundation for efficient catalytic therapy.

Just Accepted

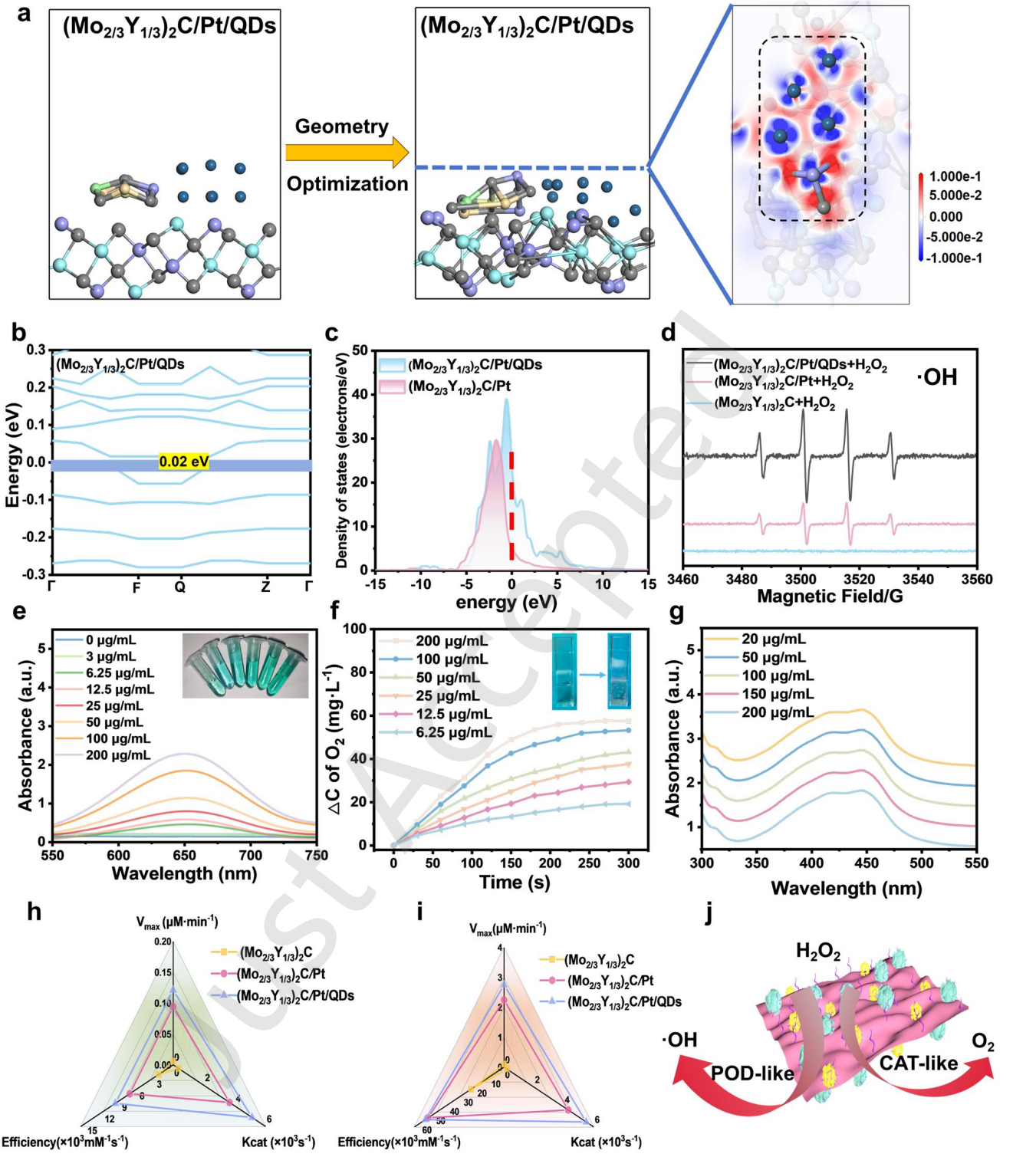


Figure 2. Electronic structure simulations, dual enzyme-mimicking activity evaluation, and kinetic analysis of $(Mo_{2/3}Y_{1/3})_2C$/Pt/QDs. (a) Differential charge density distribution and (b) band structure of $(Mo_{2/3}Y_{1/3})_2C$/Pt/QDs. (c) PDOS of $(Mo_{2/3}Y_{1/3})_2C$/Pt and $(Mo_{2/3}Y_{1/3})_2C$/Pt/QDs. (d) ESR spectra for detecting •OH radical generation. (e) Concentration-dependent POD-like activity curves of $(Mo_{2/3}Y_{1/3})_2C$/Pt/QDs (inset: photographs showing color development from 6.25 - 200 μg/mL). (f) Oxygen generation kinetic curves of $(Mo_{2/3}Y_{1/3})_2C$/Pt/QDs at different concentrations. (g) Relative enzyme activity of $(Mo_{2/3}Y_{1/3})_2C$/Pt/QDs detected using the $[Ru(dpp)_3]Cl_2$ oxygen indicator probe. (h) Radar chart of enzymatic kinetic parameters for CAT-like reactions. (i) Radar chart of enzymatic kinetic parameters for POD-like reactions. (j) Schematic illustration of the dual catalytic mechanism.

3.3 Cytotoxicity, Hemocompatibility, and Anti-Metastatic Capability Evaluation

Just Accepted

Following confirmation of the enzymatic activities of the materials, the cellular behaviors and therapeutic mechanisms of these nanocomposites were further investigated *in vitro*. Prior to cellular experiments, the surfaces of $(Mo_{2/3}Y_{1/3})_2C$, $(Mo_{2/3}Y_{1/3})_2C$/Pt, and $(Mo_{2/3}Y_{1/3})_2C$/Pt/QDs were modified with RGD tripeptide ligands to introduce active tumor-targeting capability. RGD peptides can specifically bind to $\alpha v\beta 3$ integrin receptors that are overexpressed on tumor cell surfaces, thereby enhancing cellular uptake and tumor accumulation of nanomaterials [39]. As previously described, high-entropy quantum dots primarily contribute to the enhancement of catalytic activity, whereas RGD modification mainly improves tumor-targeting ability; their synergistic effects enable efficient therapeutic performance.

To evaluate the antitumor efficacy and biosafety of the nanocomposite, systematic *in vitro* cytotoxicity and functional assays were performed. CCK-8 assay results demonstrated that cell viability in the MYPQR group exhibited a clear concentration-dependent decrease (Fig. 3a). At 100 μg/mL, cell survival declined to approximately 20%, which was significantly lower than those observed in the MoY-C and MoY-C/Pt groups, indicating that the incorporation of high-entropy quantum dots and RGD modification synergistically enhanced the antitumor activity of the nanocomposite. In sharp contrast, when evaluated on normal cell lines (LO2 human normal liver cells and HUVEC human umbilical vein endothelial cells), the nanocomposites exhibited negligible cytotoxicity, with cell viability remaining above 80% even at the highest concentration of 100 μg/mL (Fig. S12). These results demonstrate the high biocompatibility and tumor-selective killing capability of MYPQR.

Hemocompatibility is an essential safety parameter for intravenous administration. As shown in the hemolysis assays (Fig. 3b), the hemolysis rate of MYPQR stayed below 5% even at a relatively high concentration of 200 μg/mL, a level comparable to the PBS negative control group and considerably lower than the water positive control group. These observations confirmed the excellent hemocompatibility of MYPQR and indicated its suitability for intravenous administration.

Tumor metastasis represents a leading cause of cancer-related death. Transwell invasion and wound healing assays were conducted to examine how MYPQR influences the metastatic capacity of tumor cells. Relative to the PBS control group, cells treated with MYPQR exhibited markedly fewer invasive cells passing through Matrigel, showing nearly an 80% decrease in invasive cell counts by 48 h (Fig. 3c and Fig. S13). The wound healing assay (Fig. 3d and Fig. S14) further demonstrated that MYPQR treatment markedly inhibited the migration capacity of HCC-LM3 cells. After 48 h, minimal scratch closure was observed in the MYPQR-treated group, whereas control cells exhibited extensive migration into the scratched region. These findings suggest that MYPQR not only exhibits direct antitumor activity but also suppresses tumor cell invasion and migration, indicating potential anti-metastatic effects.

Just Accepted

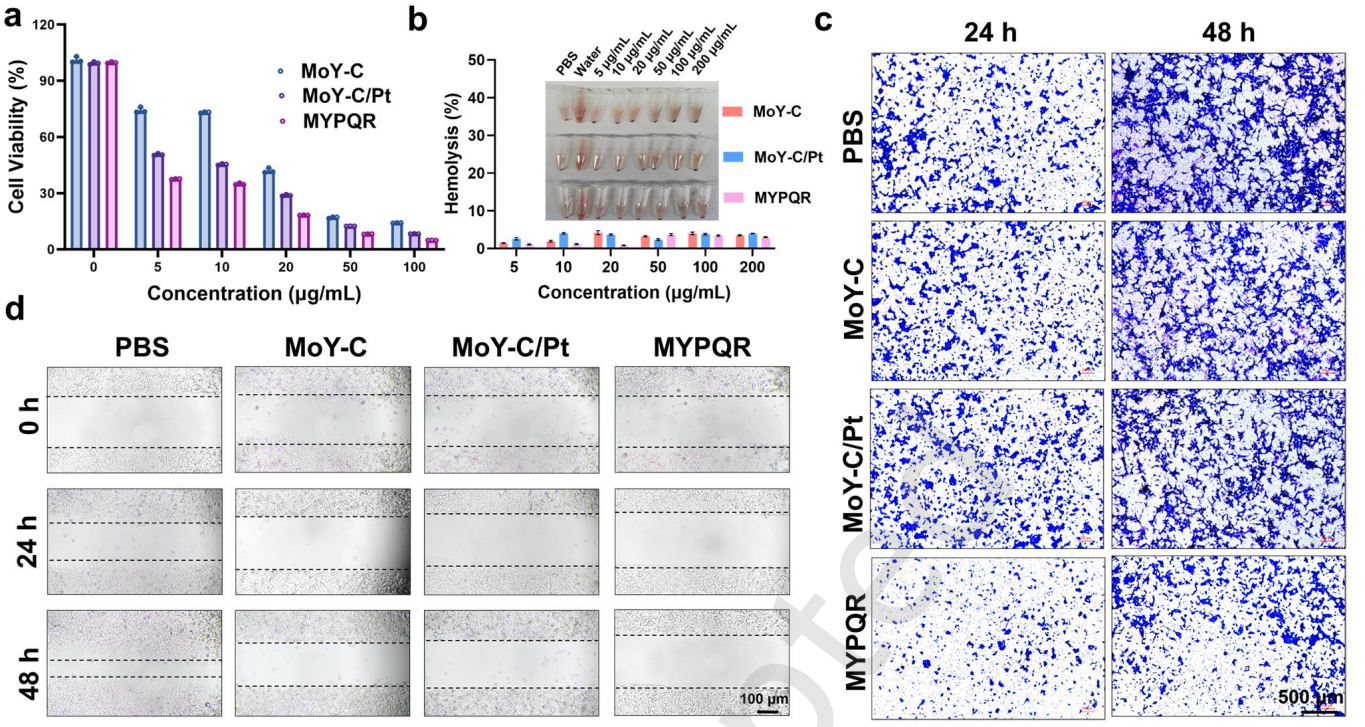


Figure 3. *In vitro* cellular validation. (a) HCC-LM3 cells were exposed to varying concentrations of materials for 24 h, and viability was determined by the CCK-8 assay. (b) Hemolysis rates at different material concentrations are shown, with representative centrifuge tube images displayed as an inset. Water and PBS served as the positive and negative controls, respectively. (c) Transwell assay evaluating cell invasion ability, with invasive cells stained purple by crystal violet. (d) Optical microscopy images of wound healing assays evaluating cell migration ability at 0, 24, and 48 h.

3.4 Cell uptake and oxidative stress induction

Due to the weak intrinsic fluorescence of HE QDs when loaded on the metallic $(Mo_{2/3}Y_{1/3})_2C$ MXene substrate, Cy5.5 was used to label the nanoplatform for fluorescence imaging and cellular tracking. CLSM images demonstrated that the MYPQR nanoplatform incorporating Cy5.5-labeled $(Mo_{2/3}Y_{1/3})_2C$ could be efficiently internalized by cancer cells in a time-dependent manner. From 3 to 12 h, the intracellular red fluorescence intensity increased progressively, indicating efficient cellular uptake of the nanocomposite (Fig. 4a). To verify whether the enhanced internalization was mediated by RGD-targeted integrin receptor interactions, a competitive inhibition experiment was performed. Compared with the unfunctionalized $(Mo_{2/3}Y_{1/3})_2C$/Pt/QDs group, the MYPQR group exhibited significantly enhanced red fluorescence, confirming the targeting capability provided by RGD modification. Furthermore, pre-incubation of cells with free RGD peptide (RGD + MYPQR group) markedly suppressed the intracellular red fluorescence signal due to competitive blocking of integrin receptors (Fig. S15). These results demonstrate that the cellular uptake of MYPQR is predominantly mediated by RGD-specific, receptor-mediated endocytosis.To evaluate intracellular ROS levels, DCFH-DA staining was performed. Compared with the PBS and MoY-C groups, cells treated with MYPQR exhibited the strongest green fluorescence intensity (Fig. 4b), accompanied by the highest percentage of DCFH-DA positive cells (Fig. 4d), confirming significantly enhanced intracellular ROS accumulation.Furthermore, the expression of hypoxia-inducible factor-1α (HIF-1α) was assessed to investigate the intracellular hypoxic status. Immunofluorescence staining revealed that the MYPQR group displayed markedly intensified green fluorescence for HIF-1α compared to the control groups (Fig. 4c), indicating pronounced intracellular hypoxia alleviation/induction and metabolic modulation.This increased oxidative stress severely disrupted the intracellular redox balance. Quantitative analysis revealed that intracellular GSH levels were markedly reduced in the MYPQR group, suggesting effective depletion of the antioxidant defense system (Fig. 4e). Consequently, enhanced oxidative damage to cellular macromolecules was observed, as indicated by elevated levels of 8-OHdG, a marker of oxidative DNA damage (Fig. 4f), and increased malondialdehyde (MDA), a representative

Just Accepted

indicator of lipid peroxidation (Fig. 4g). These findings demonstrate that MYPQR effectively induces cellular oxidative stress, modulates hypoxic signaling, and promotes cell damage in cancer cells.

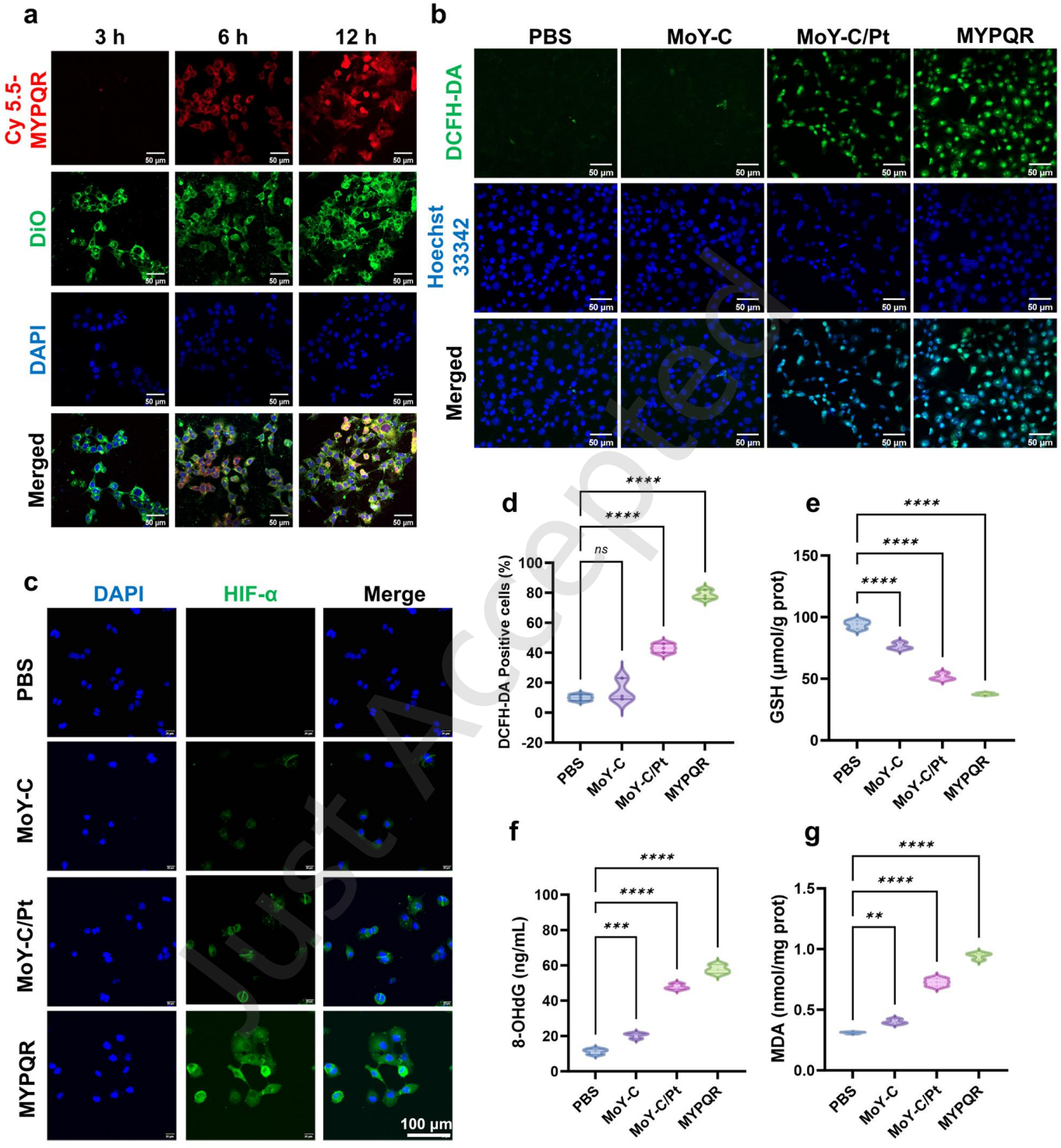


Figure 4. Cellular uptake and oxidative stress induction by the MYPQR nanocomposite. (a) CLSM images showing the uptake of Cy5.5-labeled MYPQR in HCC-LM3 cells after different incubation times (3, 6, and 12 h). (b) DCFH-DA fluorescence images showing intracellular ROS generation in HCC-LM3 cells after different treatments. (c) Immunofluorescence staining of HIF-1α expression in cells subjected to different treatments. (d) Quantitative analysis of DCFH-DA positive cells (%). (e) Intracellular GSH levels. (f) Content of the oxidative DNA damage marker 8-OHdG. (g) Cellular MDA levels, representing lipid peroxidation, after treatment with different materials. (****P < 0.0001).

Just Accepted

3.5 Mitochondrial function and glucose metabolic enzyme activity analysis

To systematically elucidate the subcellular behavior and energy metabolism interference mechanism of MYPQR, mitochondrial targeting, lysosomal escape, and metabolic pathways were comprehensively investigated. First, the intracellular transport pathway of Cy5.5-labeled MYPQR was monitored using Lyso-Tracker staining (Fig. 5a). Over time (2 - 8 h), the red fluorescence of MYPQR progressively separated from the green lysosomal signal, demonstrating successful lysosomal escape primarily driven by the proton sponge effect. Subsequently, driven by its lipophilic cationic nature and the strongly negative inner mitochondrial membrane potential (ΔΨm), the escaped MYPQR selectively targeted and accumulated in mitochondria, as confirmed by strong co-localization with Mito-Tracker (Fig. 5b). To evaluate mitochondrial dysfunction induced by localized MYPQR accumulation, mitochondrial membrane potential (ΔΨm) was assessed using JC-1 staining (Fig. 5c). The PBS control group exhibited intense red fluorescence derived from JC-1 aggregates, indicating intact ΔΨm. In sharp contrast, cells treated with MYPQR displayed predominant green fluorescence corresponding to JC-1 monomers, demonstrating severe collapse of ΔΨm following treatment.Given the tight coupling between mitochondrial function and cellular energy production, the impact of MYPQR on tumor cell glycolytic activity (Warburg effect) was further examined. MYPQR treatment markedly suppressed aerobic glycolysis. Specifically, the activity of hexokinase (HK), a key rate-limiting enzyme in glycolysis, was dramatically reduced (Fig. 5d). Consequently, intracellular glucose (Glu) consumption/uptake (Fig. 5e) and lactate (LA) production (Fig. 5f) were substantially decreased. Ultimately, the combined disruption of mitochondrial integrity and glycolytic pathways led to a catastrophic drop in intracellular ATP levels (Fig. 5g). Taken together, these findings demonstrate that MYPQR effectively escapes lysosomes, targets mitochondria, and severely impairs tumor cellular energy homeostasis.

Just Accepted

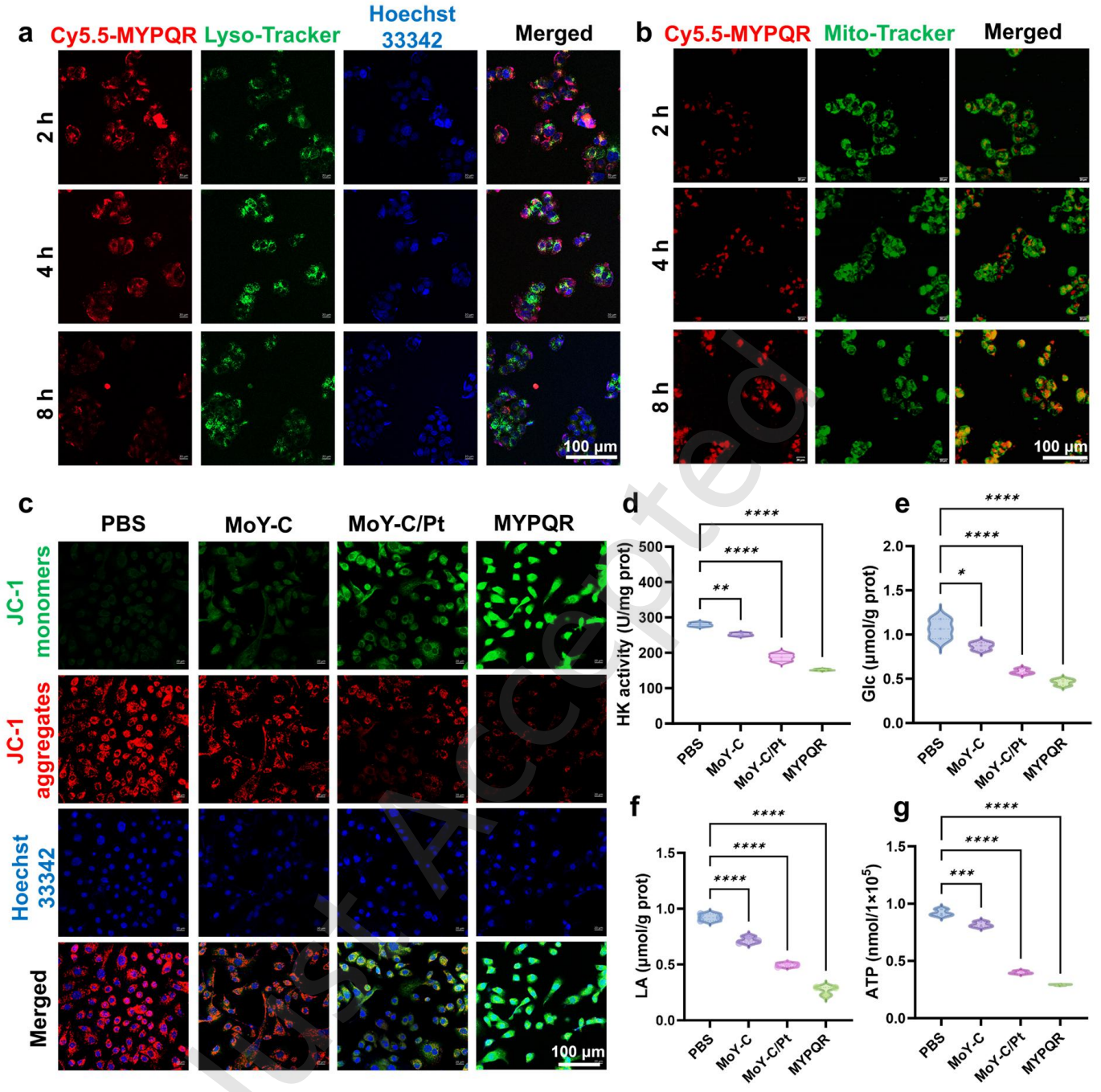


Figure 5. Subcellular organelle targeting, lysosomal escape, and inhibition of tumor energy metabolism by MYPQR. (a) CLSM images illustrating lysosomal escape of Cy5.5-MYPQR (red) co-stained with Lyso-Tracker (green) and Hoechst 33342 (blue) at 2, 4, and 8 h. (b) CLSM images showing the time-dependent mitochondrial targeting of Cy5.5-MYPQR (red) co-stained with Mito-Tracker (green) at 2, 4, and 8 h. (c) Fluorescence microscopy images showing JC-1-labeled cells under various treatment conditions (scale bar: 100 μm). Red fluorescence denotes elevated mitochondrial membrane potential (JC-1 aggregates), whereas green fluorescence denotes diminished mitochondrial membrane potential (JC-1 monomers). (d-g) Quantitative analysis of cellular energy metabolism-related indicators: (d) HK activity; (e) intracellular Glu content; (f) LA content; (g) intracellular ATP levels. (****P < 0.0001).

3.6 *In vitro* anti-tumor efficacy and biosafety evaluation

Subsequently, the in vivo targeted accumulation and therapeutic efficacy of MYPQR were systematically evaluated in HCC-LM3 tumor-bearing mouse models. The biodistribution of Cy5.5-labeled nanocomposites was monitored via real-time in vivo fluorescence imaging. The Cy5.5-MYPQR group exhibited significantly stronger fluorescence signals at the tumor site compared to the non-RGD-

Just Accepted

functionalized Cy5.5-($Mo_{2/3}Y_{1/3}$)$_2$C/Pt/QDs group (Fig. 6a). Ex vivo imaging of major organs and tumors harvested at 36 h post-injection further verified that Cy5.5-MYPQR achieved markedly superior tumor accumulation and retention compared with the non-targeting counterpart (Fig. 6b-c). Quantitative fluorescence analysis confirmed the time-dependent tumor targeting capability (Fig. 6d) and significantly elevated tumor-to-normal tissue signal ratios (T/N ratio) (Fig. 6e), as well as the enhanced organ and tumor tissue biodistribution of MYPQR (Fig. 6f). Encouraged by its outstanding tumor-targeting performance, the in vivo antitumor therapeutic efficacy was evaluated over a 14-day treatment period. Digital photographs of excised tumors at the end of treatment intuitively showed the smallest tumor sizes in the MYPQR group (Fig. 6g). Tumor growth curves demonstrated that tumor progression was almost completely suppressed in MYPQR-treated mice (Fig. 6h), which was further corroborated by the lowest average tumor weights (Fig. 6i). Histological and immunofluorescence evaluations of tumor tissue sections further unraveled the therapeutic mechanism. H&E staining revealed severe tissue necrosis, cellular atrophy, and nuclear disintegration in the MYPQR group (Fig. 6j). Ki67 immunofluorescence staining confirmed a significant reduction in cell proliferation (Fig. 6j, k), while TUNEL fluorescence staining demonstrated a substantial increase in cell apoptosis (Fig. 6j, l).Furthermore, systemic in vivo biosafety was comprehensively verified. No significant loss of body weight was recorded across any treatment group over 14 days (Fig. S16). H&E staining of major organs (lung, liver, spleen, kidney, and heart) showed no observable pathological alterations or tissue damage (Fig. S17). Additionally, standard hematological parameters and serum biochemical markers for renal (BUN, CREA) and liver (LDH, AST, ALT) functions remained within normal physiological ranges, confirming the excellent systemic biocompatibility and high safety profile of MYPQR(Fig. S18). These results collectively confirm that the quantum dot-enhanced catalytic nanoplatform can effectively eradicate tumors in vivo by inducing severe oxidative stress and metabolic failure.

Just Accepted

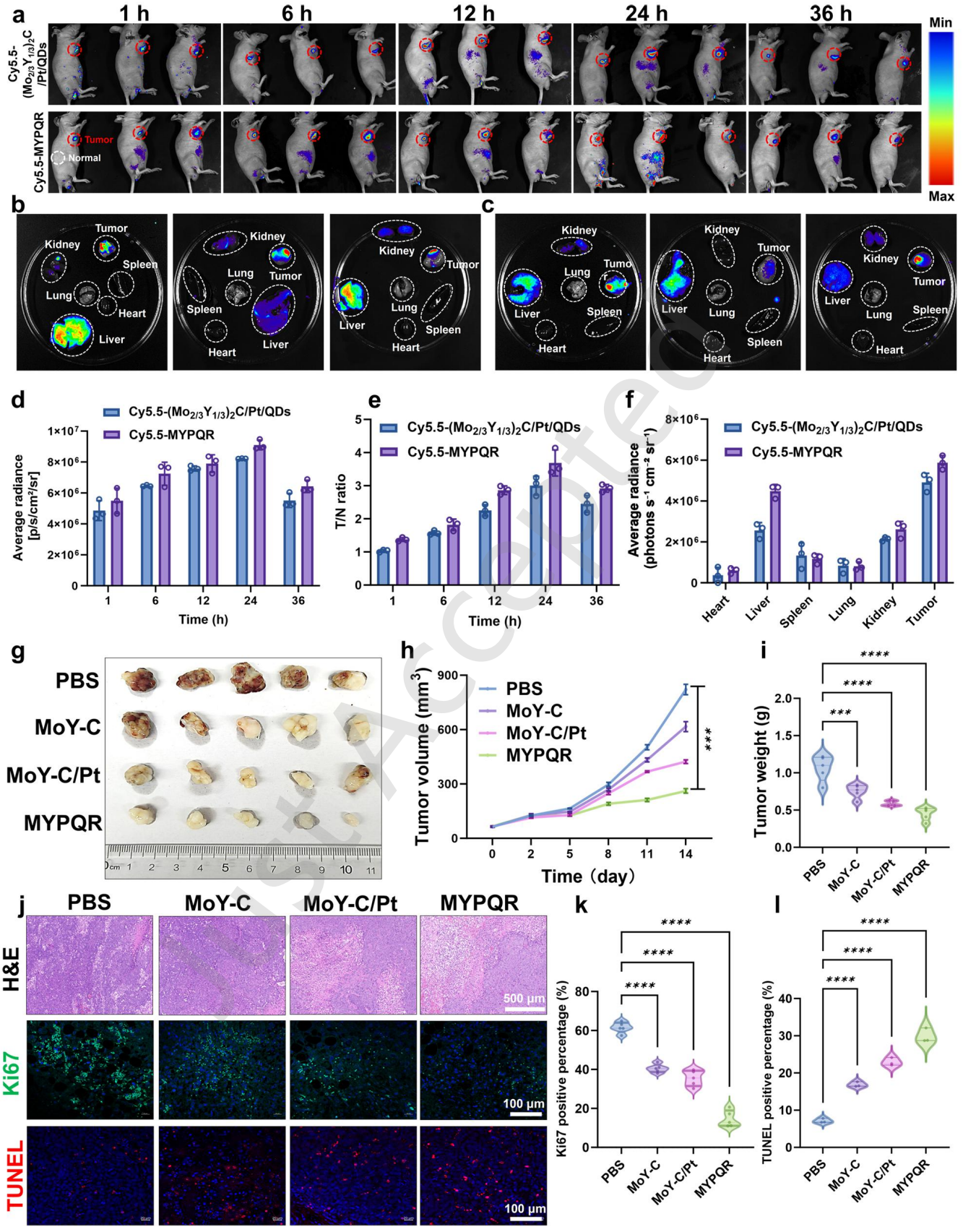


Figure 6. *In vivo* biodistribution, tumor targeting, and therapeutic efficacy of MYPQR in HCC-LM3 tumor-bearing mice. (a) In vivo fluorescence images of tumor-bearing mice at indicated time intervals (1, 6, 12, 24, and 36 h) after intravenous injection of Cy5.5-$(Mo_{2/3}Y_{1/3})_2C$/Pt/QDs or Cy5.5-MYPQR (red circles denote tumor sites; white circles denote normal tissues). Ex vivo fluorescence images of major organs (heart, liver, spleen, lungs, kidneys) and tumors harvested at 36 h post-injection from mice treated with (b) Cy5.5-$(Mo_{2/3}Y_{1/3})_2C$/Pt/QDs and (c) Cy5.5-MYPQR. (d) Quantitative average radiance of tumor sites at different time points. (e) T/N

ratio calculated at corresponding time intervals. (f) Quantitative average radiance of harvested major organs and tumors. (g) Photographs depicting excised tumors collected from each treatment group at day 14 post-treatment. (h) Tumor growth trends recorded for mice in each treatment group throughout the treatment course. (i) The weight of tumors in each group of mice after the treatment was completed. (j) Representative images of H&E staining (histological morphology), Ki67 immunofluorescence staining (green, proliferation assessment), and TUNEL immunofluorescence staining (red, apoptosis assessment) of tumor tissues (scale bars indicated in images). Quantitative analysis of (k) Ki67-positive rate and (l) TUNEL-positive rate based on immunofluorescence staining. (***P < 0.001, ****P < 0.0001).

3.7 Global Metabolic Reprogramming Triggered by $(Mo_{2/3}Y_{1/3})_2C$/Pt/QDs/RGD

To elucidate the therapeutic mechanisms associated with progressive component optimization, matrix-assisted laser desorption/ionization time-of-flight mass spectrometry imaging (MALDI-TOF MSI) was performed to investigate the spatial distribution and relative abundance of key tumor-associated metabolites. In the untreated PBS group, MSI analysis revealed a pathological metabolic profile characteristic of active liver malignancy, with dysregulated distribution patterns of tumor-associated metabolites. Treatment with bare MoY-C induced pronounced metabolic alterations, as evidenced by irregular and enhanced peripheral metabolic signals, suggesting strong localized metabolic effects. The incorporation of Pt nanoparticles into MoY-C/Pt moderated these metabolic changes and resulted in a more balanced metabolic response. Notably, the multi-component MYPQR nanoplatform, equipped with high-entropy QDs and RGD-mediated active targeting, achieved a more uniform and regulated metabolic profile.

Detailed analysis of individual metabolic pathways further demonstrated the metabolic regulatory effects of MYPQR. For L-arginine (Fig. 7a), the reduced metabolic signal associated with the immunosuppressive TME in the PBS and MoY-C groups was partially restored following MYPQR treatment, suggesting improved regulation of the tumor metabolic state. For adenosine cyclophosphate (cAMP) (Fig. 7b), the excessive accumulation and heterogeneous distribution observed in the control groups were reduced and normalized following MYPQR treatment, yielding a more uniform spatial distribution pattern. Similarly, the distribution of fructose-1,6-bisphosphate (Fig. 7c) indicated that MYPQR treatment modulated glycolytic metabolism and improved metabolic homeostasis. Furthermore, the altered distribution of glycodeoxycholic acid (Fig. 7d) suggested that MYPQR influenced dysregulated lipid and bile acid metabolism associated with tumor progression. Finally, the elevated signals of uridine triphosphate (UTP) (Fig. 7e), which is involved in nucleic acid synthesis during cancer cell proliferation, were reduced and homogenized after MYPQR treatment, indicating suppression of proliferative metabolic activity. Collectively, these MALDI-TOF MSI results demonstrate that MYPQR regulates tumor-associated metabolic alterations through coordinated modulation of multiple metabolic pathways, contributing to its enhanced antitumor efficacy.

Just Accepted

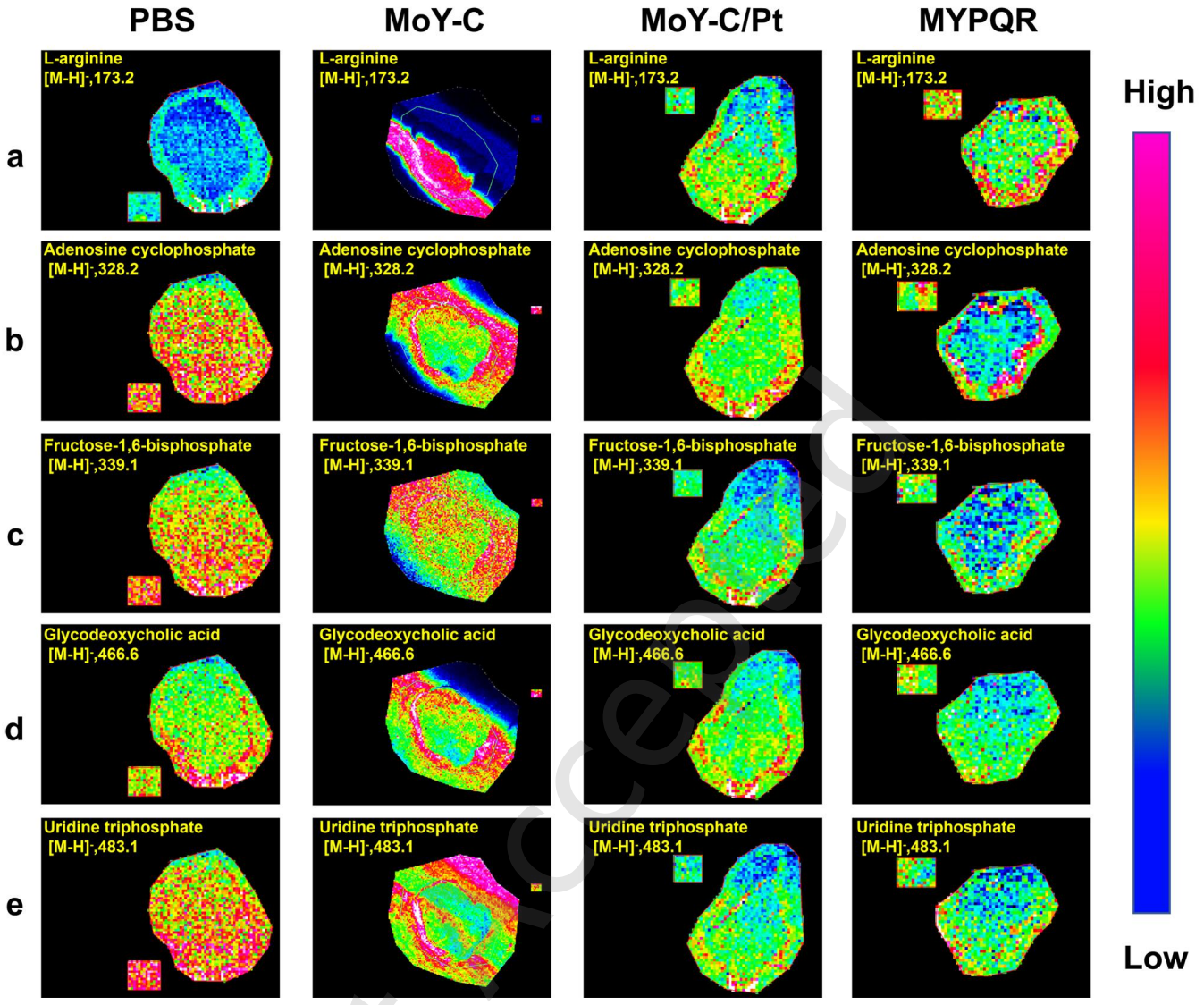


Figure 7. MALDI-TOF MSI images of differentially distributed metabolites in tumor tissues: (a) L-arginine, 174.201 m/z; (b) adenosine cyclophosphate, 329.206 m/z; (c) fructose-1,6-bisphosphate, 340.116 m/z; (d) glycodeoxycholic acid, 467.639 m/z; (e) uridine triphosphate, 484.141 m/z.

4 Conclusions

In summary, this study developed a multi-component $(Mo_{2/3}Y_{1/3})_2C$/Pt/QDs/RGD nanoplatform that integrates targeted delivery and nanocatalytic activity for HCC therapy. The incorporation of high-entropy quantum dots and RGD peptides onto the MXene substrate endowed the system with active tumor-targeting capability and cascade enzyme-mimicking activities, including CAT-like and POD-like activities. DFT calculations demonstrated that interfacial electronic interactions and the upward shift of the Pt d-band center contributed to optimized catalytic kinetics. Combined with spatial metabolomic analyses, this study revealed that tumor suppression was associated with coordinated metabolic regulation, including restoration of dysregulated metabolite profiles and inhibition of aberrant metabolic activity, rather than nonspecific cytotoxic effects. Overall, this work provides a potential design strategy for developing microenvironment-responsive nanocatalytic systems for tumor therapy.

Electronic Supplementary Material: Supplementary material (please provide the brief detail of the ESM) is available in the onlineversion of this article at https://doi.org/10.26599/NR.2026.94909208.

Data availability

All data generated and analyzed during this study are included in the article and its Supplementary Information files and are also available from the corresponding author upon reasonable request. Source data are provided with this article.

Just Accepted

Acknowledgements
This work was supported by the Jiangsu Provincial Research Hospital (YJXYY202204-YSB76 for Feiran Wang) and the Natural Science Foundation of Hubei Province (2020CFB712 for Yong Qiang).

Declaration of competing interest
The authors declare that they have no competing interests.

Author contribution statement
X. X. and W. F. conceived and designed the experiments. X. X. performed the experiments with support from L. X. S. W. performed the data analysis. W. F. and Q. Y. provided supervision and project management. X. X. drafted the manuscript. All authors contributed to the discussion and approved the final manuscript.

Informed consent
Not applicable.

Ethics statement
All animal experiments were approved by the Animal Ethics Committee of Nantong University (IACUC20230721-002).

Use of AI statement
None.

References

[1] Sankar K, Gong J, Osipov A, et al. Recent advances in the management of hepatocellular carcinoma. *CMH* **2024**, *30*, 1–15.
[2] Moris D, Martinino A, Schiltz S, et al. Advances in the treatment of hepatocellular carcinoma: An overview of the current and evolving therapeutic landscape for clinicians. *CA: A Cancer Journal for Clinicians* **2025**, *75*, 498–527.
[3] Cabibbo G, Rimassa L, Lamarca A, et al. The present and the future of immunotherapy in hepatocellular carcinoma and biliary tract cancers. *Cancer Treatment Reviews* **2025**, *137*.
[4] Su X, Yan X,Zhang H The tumor microenvironment in hepatocellular carcinoma: mechanistic insights and therapeutic potential of traditional Chinese medicine. *Molecular Cancer* **2025**, *24*, 173.
[5] Singal AG, Salem R, Pinato DJ, et al. Advances in Locoregional and Systemic Treatments for Hepatocellular Carcinoma. *Gastroenterology* **2025**, *169*, 585–599.
[6] Pinter M, Fulgenzi CAM, Pinato DJ, et al. Systemic treatment in patients with hepatocellular carcinoma and advanced liver dysfunction. *Gut* **2025**, *74*, 1178.
[7] Dai S, Chen Y, Cai W, et al. Combination immunotherapy in hepatocellular carcinoma: synergies among immune checkpoints, TKIs, and chemotherapy. *Journal of Hematology & Oncology* **2025**, *18*, 85.
[8] Malik AK, Geh D, Jeffry Evans TR, et al. Improving surgical treatments for hepatocellular carcinoma. *Nature Reviews Gastroenterology & Hepatology* **2026**, *23*, 208–226.
[9] Vogel A, Grant RC, Meyer T, et al. Adjuvant and neoadjuvant therapies for hepatocellular carcinoma. *Hepatology* **2025**, *82*.
[10] Tang Z, Ou Y, Wang Y, et al. A dual responsive hydrogel with a single-atom copper nanodrug for precision and sustained tumor therapy. *Journal of Materials Chemistry B* **2026**, *14*, 4144–4157.
[11] Liu R, Feng J, Chen Q, et al. A nanoplatform with H_2O_2 self-supplying capability for synergistic chemo/enzyme dynamic/chemodynamic therapy of ovarian cancer. *Journal of Materials Chemistry B* **2025**, *13*, 14773–14783.
[12] Li L, Liu A, Wang Z, et al. Biomimetic cascade "four-in-one" Nanozyme for remodeling the redox tumor microenvironment and disrupting energy homeostasis to enhance ferroptosis against triple-negative breast cancer. *Biomaterials* **2026**, *330*, 124001.
[13] Xu M, Yang Y,Yuan Z Breast Cancer Cell Membrane Camouflaged Lipid Nanoparticles for Tumor-Targeted NIR-II Phototheranostics. *Pharmaceutics* **2022**, *14*.
[14] Guan Y, Xing C, Tong T, et al. Smart dual responsive nanocarriers with reactive oxygen species amplification assisted synergistic chemotherapy against prostate cancer. *Journal of Colloid and Interface Science* **2022**, *622*, 789–803.
[15] Chen H, Wang M, Yang Q, et al. Multifunctional porphyrinic metal-organic framework-based nanoplatform regulating reactive oxygen species achieves efficient imaging-guided cascaded nanocatalytic therapy. *Journal of Colloid and Interface Science* **2025**, *684*, 423–438.
[16] Wang Q, Du J, Yang F, et al. Charge Separation-Engineered Piezoelectric Ultrathin Nanorods Modulate Tumor Stromal Microenvironment and Enhance Cell Immunogenicity for Synergistically Piezo-Thermal-Immune Therapy. *Small* **2025**, *21*, 2408038.
[17] Gao N, Zhao J, Zhu X, et al. Functional two-dimensional MXenes as cancer theranostic agents. *Acta Biomaterialia* **2022**, *154*, 1–22.
[18] Gao P, Wei R, Chen Y, et al. Pt nanozyme-bridged covalent organic framework-aptamer nanoplatform for tumor targeted self-strengthening photocatalytic therapy. *Biomaterials* **2023**, *297*, 122109.
[19] Liu H, Lei S, Li H, et al. Refining Single-Atom Catalytic Kinetics for Tumor Homologous-Targeted Catalytic Therapy. *Nanomicro Lett* **2025**, *17*, 253.
[20] Yang P, Tao J, Chen F, et al. Multienzyme-Mimic Ultrafine Alloyed Nanoparticles in Metal Organic Frameworks for Enhanced Chemodynamic Therapy. *Small* **2021**, *17*, e2005865.
[21] Wu J, Wei Y, Lan J, et al. Screening of Protein-Based Ultrasmall Nanozymes for Building Cell-Mimicking Catalytic Vesicles. *Small* **2022**, *18*, 2202145.

Just Accepted

[22] Ye Y, Yu H, Chen B, et al. Engineering nanoenzymes integrating Iron-based metal organic frameworks with Pt nanoparticles for enhanced Photodynamic-Ferroptosis therapy. *Journal of Colloid and Interface Science* **2023**, *645*, 882–894.
[23] Zhu Y, Wang Z, Zhao R, et al. Pt Decorated $Ti_3C_2T_x$ MXene with NIR-II Light Amplified Nanozyme Catalytic Activity for Efficient Phototheranostics. *ACS Nano* **2022**, *16*, 3105–3118.
[24] Shen M, Xie L, Zhang Y, et al. Molecular engineering and channel structure modulation for single-atom iron-embedded high-porosity carbon fibers with enhanced oxygen reduction reaction and zinc-air battery performance. *Journal of Colloid and Interface Science* **2025**, *699*, 138230.
[25] Enoch K, Sundaram A, Ponraj SS, et al. Enhancement of MXene optical properties towards medical applications via metal oxide incorporation. *Nanoscale* **2023**, *15*, 16874–16889.
[26] Wan B, Liu N, Zhang Z, et al. Water-dispersible and stable polydopamine coated cellulose nanocrystal-MXene composites for high transparent, adhesive and conductive hydrogels. *Carbohydr Polym* **2023**, *314*, 120929.
[27] Zhong H, Huang P-Y, Yan P, et al. Versatile Nanodrugs Containing Glutathione and Heme Oxygenase 1 Inhibitors Enable Suppression of Antioxidant Defense System in a Two-Pronged Manner for Enhanced Photodynamic Therapy. *Advanced Healthcare Materials* **2021**, *10*, 2100770.
[28] Zuo W, Fan Z, Chen L, et al. Copper-based theranostic nanocatalysts for synergetic photothermal-chemodynamic therapy. *Acta Biomaterialia* **2022**, *147*, 258–269.
[29] Li Y, Han S, Zhao Y, et al. A Redox-Triggered Polymeric Nanoparticle for Disrupting Redox Homeostasis and Enhanced Ferroptosis. *Small* **2025**, *21*, 2404299.
[30] Liu K, Liu X, Wen L, et al. Blocking Metallothionein-2 Expression by Copper-Doped Carbon Dots Induces Cellular Antioxidant System Collapse for Antitumor Therapy. *Nano Letters* **2024**, *24*, 10699–10709.
[31] Tang Q, Wang Y, Chen N, et al. Ultra-Efficient Synthesis of $Nb_4C_3T_x$ MXene via H_2O-Assisted Supercritical Etching for Li-Ion Battery. *Small Methods* **2024**, *8*, 2300836.
[32] Xu W, Wu Q, Gwon J, et al. Ice-Crystal-Templated "Accordion-Like" Cellulose Nanofiber/MXene Composite Aerogels for Sensitive Wearable Pressure Sensors. *ACS Sustain Chem Eng* **2023**, *11*, 3208–3218.
[33] Li X, Yu J, Jin T, et al. Defect-Engineered $CoSe_2$ Quantum Dots Exposing Highly Active (111) Facets with Lithiophilic-Sulfurophilic Functionality for High-Energy Lithium–Sulfur Batteries. *Advanced Science* **2026**, *13*, e11623.
[34] Huang Y, Lv J, Gu L, et al. Atomic Layer Deposition-Derived MoS_2/NbS_2 Nanoheterojunctions Enable High-Density Quantum Dot Loading for Enhanced Signal-On Photoelectrochemical Detection of cTnI. *ACS Appl Mater Interfaces* **2025**, *17*, 49020–49028.
[35] Sheng J, He Y, Li J, et al. Identification of Halogen-Associated Active Sites on Bismuth-Based Perovskite Quantum Dots for Efficient and Selective CO_2-to-CO Photoreduction. *ACS Nano* **2020**, *14*, 13103–13114.
[36] Bischoff NS, Undas AK, van Herwijnen M, et al. E171-induced toxicity in human iPSC-derived colon organoids: Effects on cell viability, ROS generation, DNA damage, and gene expression changes. *Toxicol In Vitro* **2025**, *108*, 106105.
[37] Faizullin BA, Dayanova IR, Kurenkov AV, et al. ROS-producing nanomaterial engineered from Cu(I) complexes with P_2N_2-ligands for cancer cells treating. *Discov Nano* **2023**, *18*, 133.
[38] Wang J, Zhang S, Wang Q, et al. Aptamer modified NPA hollow nanozymes with intrinsic peroxidase-like activity for colorimetric sensing of H1N1. *Analytica Chimica Acta* **2026**, *1402*, 345189.
[39] Ma L, Niu M, Ji Y, et al. Development of KLA-RGD integrated lipopeptide with the effect of penetrating membrane which target the αvβ3 receptor and the application of combined antitumor. *Colloids and Surfaces B: Biointerfaces* **2023**, *223*, 113186.

© The Author(s) 2026. *Nano Research* published by Tsinghua University Press. The articles published in this open access journal are distributed under the terms of the Creative Commons Attribution 4.0 International License (http://creativecommons.org/licenses/by/4.0/), which permits use, distribution and

Just Accepted

Electronic Supplementary Material

High-entropy quantum dots-modulated Pt/MXene heterojunction nanozymes for targeted catalytic therapy of hepatocellular carcinoma

Xiaodong Xu[1,§], Xiancheng Liu[2,§], Weiwei Shao[3], Yong Qiang[4], and Feiran Wang[5]

[1] *Department of General Surgery, The First People's Hospital of Yancheng, Yancheng 224000, China*
[2] *Department of Radiation Oncology, Affiliated Hospital of Nantong University, Nantong 226000, China*
[3] *Department of Hepatobiliary Surgery, Beijing Chao-Yang Hospital affiliated to Capital Medical University, Beijing 100023, China*
[4] *Department of Hepatobiliary Surgery, JingMen People's Hospital, Jingchu University of Technology Affiliated JingMen People's Hospital, JingMen 448000, China*
[5] *Department of General Surgery, Affiliated Hospital of Nantong University, Nantong 226000, China*
[§] *Xiaodong Xu and Xiancheng Liu contributed equally to this work.*

Address correspondence to wangfeirangs@ntu.edu.cn

Supporting information to https://doi.org/10.26599/NR.2026.94909208

Just Accepted

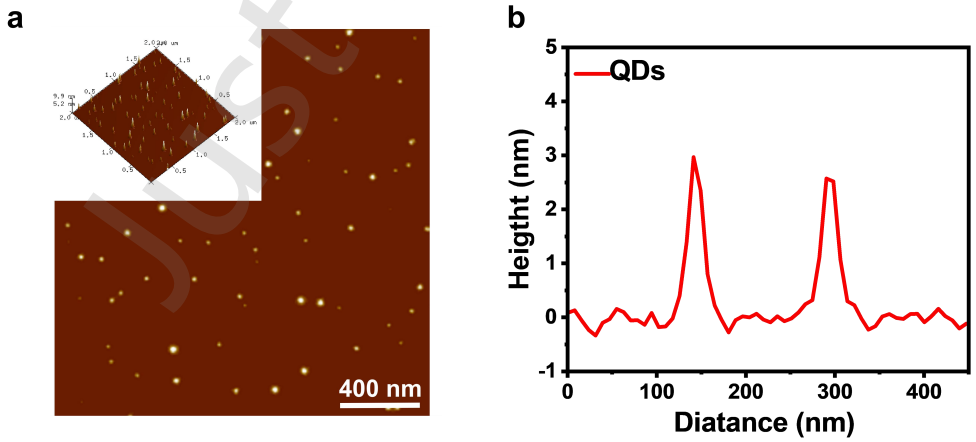


Figure S1. (a) AFM image of QDs and (b) corresponding height distribution profile.

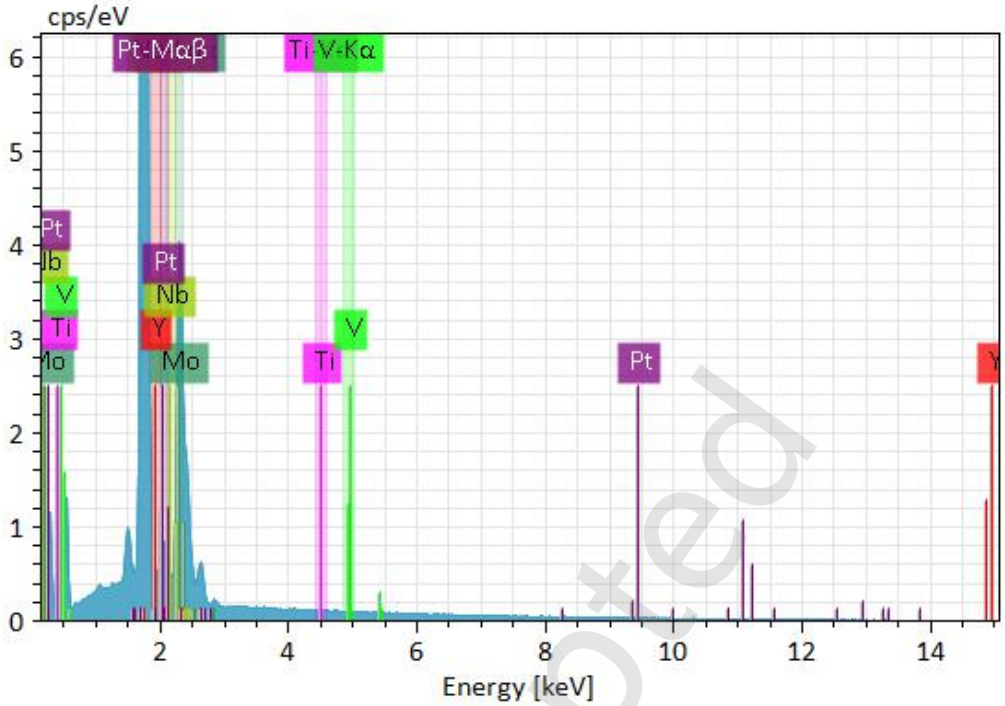


Figure S2. Element distribution map of $(Mo_{2/3}Y_{1/3})_2C$/Pt/QDs.

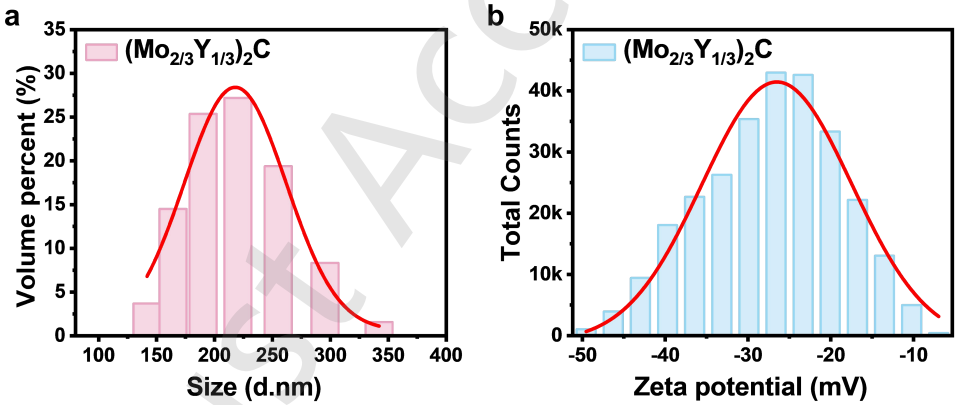


Figure S3. (a) Hydrodynamic size distribution and (b) Zeta potential distribution of $(Mo_{2/3}Y_{1/3})_2C$.

Just Accepted

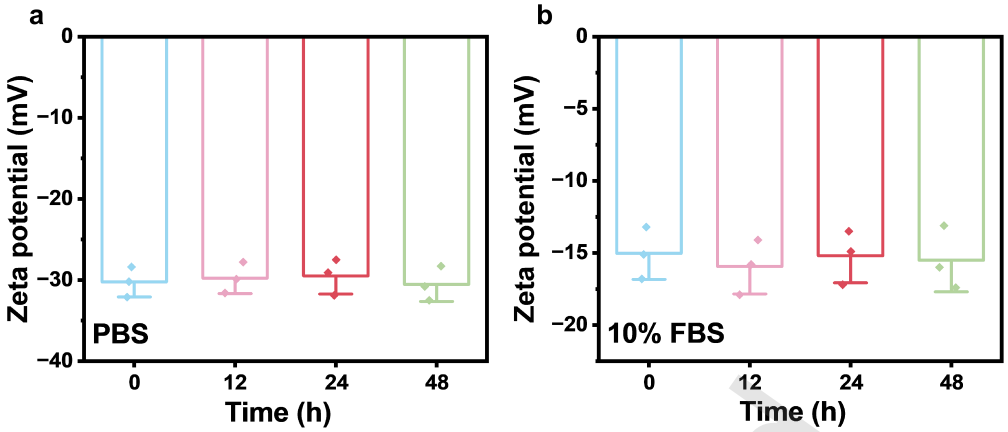


Figure S4. Time-dependent zeta potential and colloidal stability of $(Mo_{2/3}Y_{1/3})_2C$/Pt/QDs in (a) PBS and (b) 10% FBS.

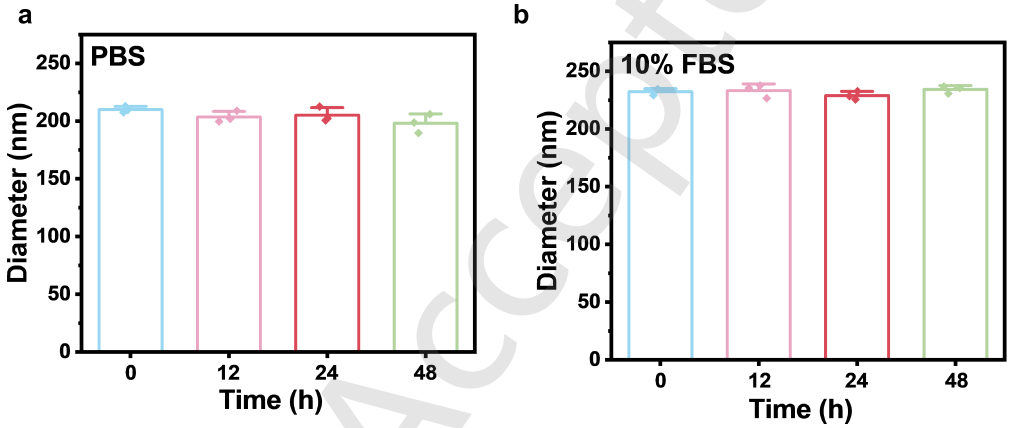
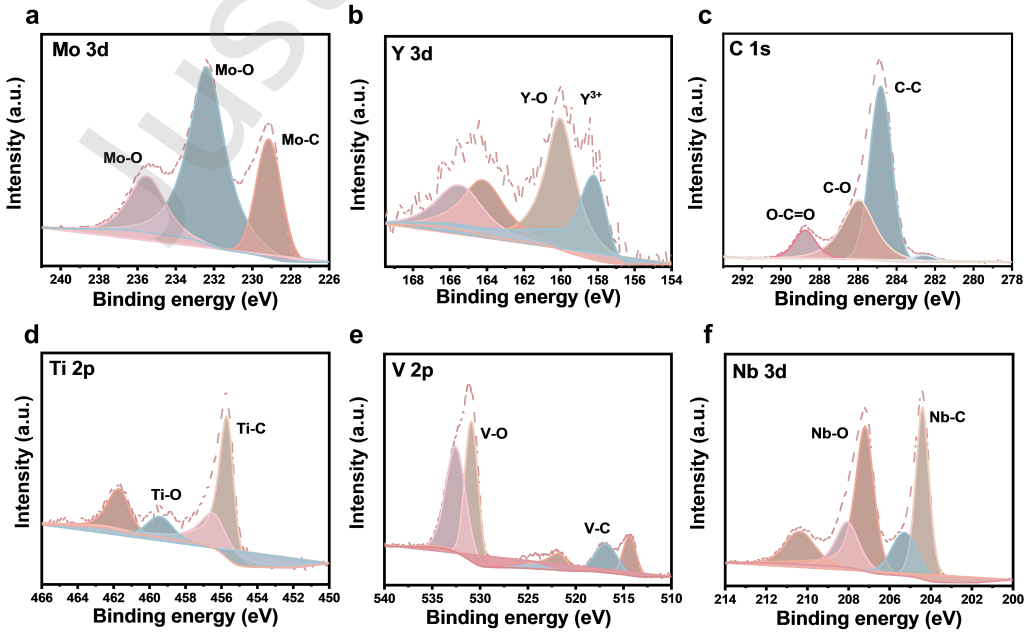


Figure S5. Time-dependent hydrodynamic size and colloidal stability of $(Mo_{2/3}Y_{1/3})_2C$/Pt/QDs in (a) PBS and (b) 10% FBS.



Just Accepted

Figure S6. High-resolution XPS spectra of (a) Mo 3d, (b) Y 3d, (c) C 1s, (d) Ti 2p, (e) V 2p and (f) Nb 3d.

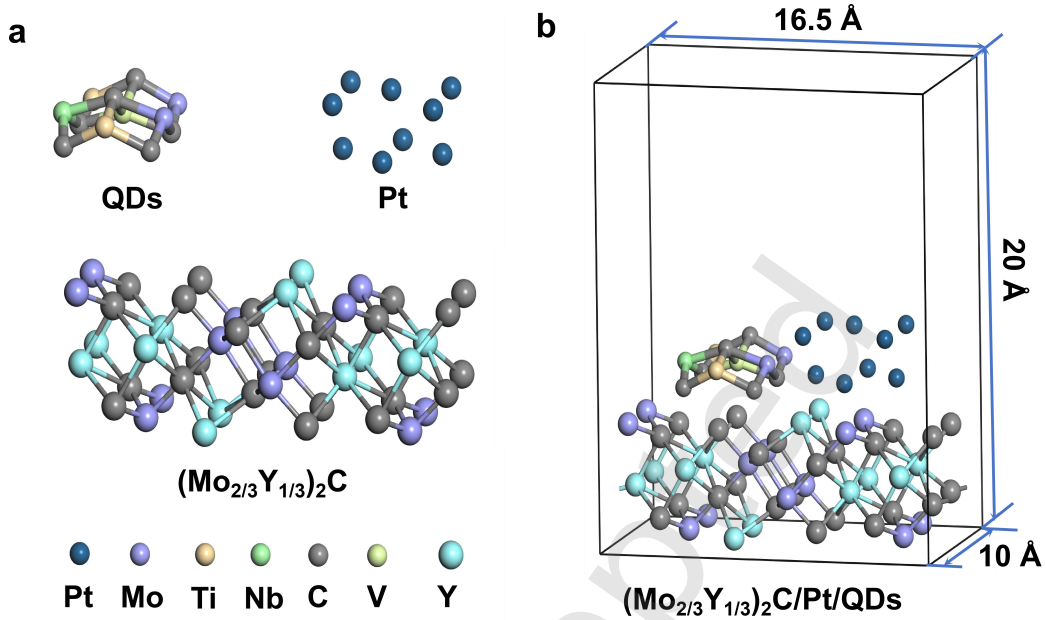


Figure S7. The DFT calculation model of (a) QDs, Pt, $(Mo_{2/3}Y_{1/3})_2C$ and (b) $(Mo_{2/3}Y_{1/3})_2C$/Pt/QDs.

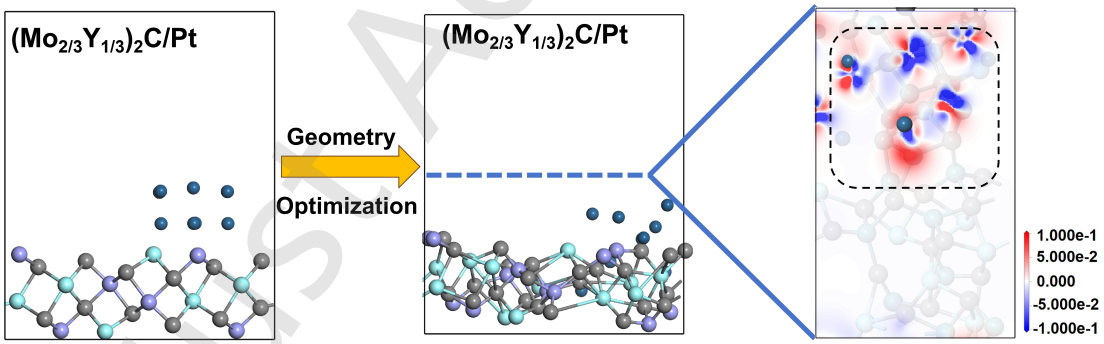


Figure S8. The differential charge density distribution of $(Mo_{2/3}Y_{1/3})_2C$/Pt.

Just Accepted

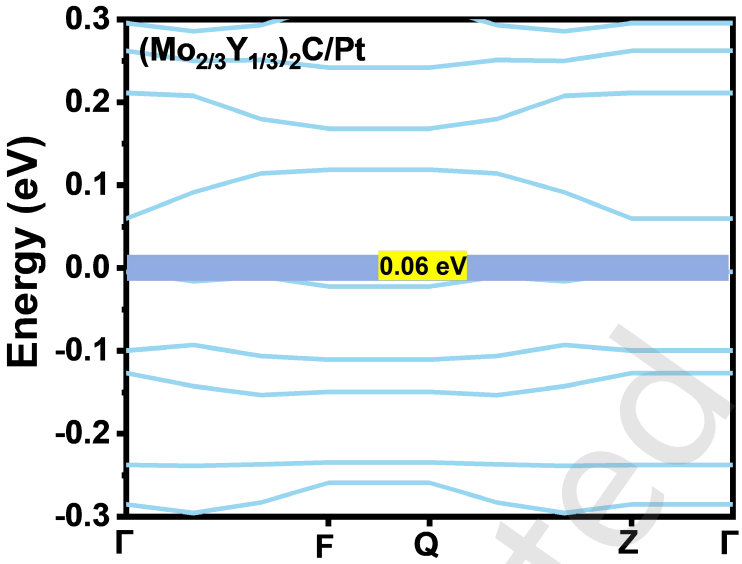


Figure S9. PDOS of $(Mo_{2/3}Y_{1/3})_2C$/Pt.

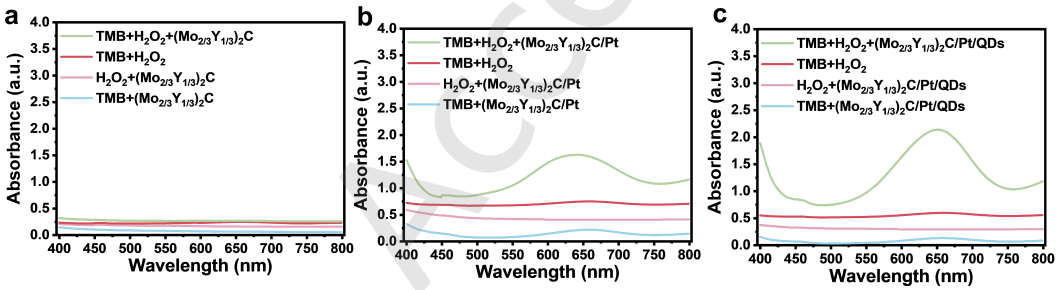


Figure S10. UV-vis absorption spectra of (a) $(Mo_{2/3}Y_{1/3})_2C$, (b) $(Mo_{2/3}Y_{1/3})_2C$/Pt and (c) $(Mo_{2/3}Y_{1/3})_2C$/Pt/QDs at the same concentration (200 μg/mL) in the TMB-H_2O_2 system.

Just Accepted

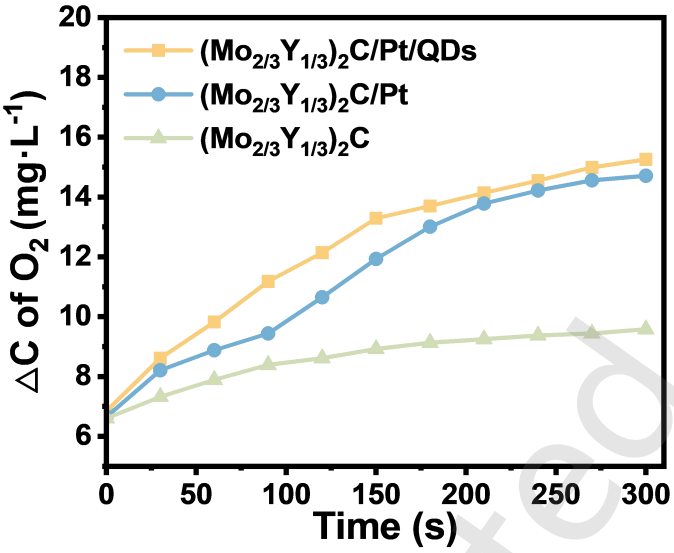


Figure S11. Time-course curves of oxygen generation from H_2O_2 decomposition catalyzed by different materials at the same concentration.

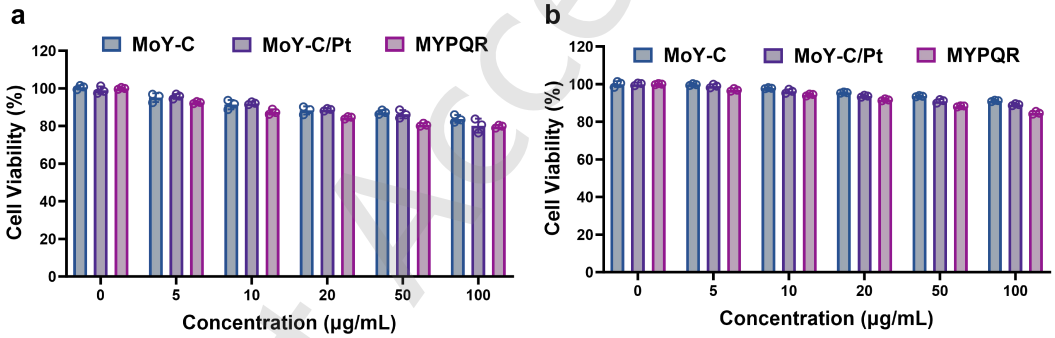


Figure S12. In vitro cytotoxicity and biosafety evaluation in (a) L02 and (b) HUVEC cells.

Just Accepted

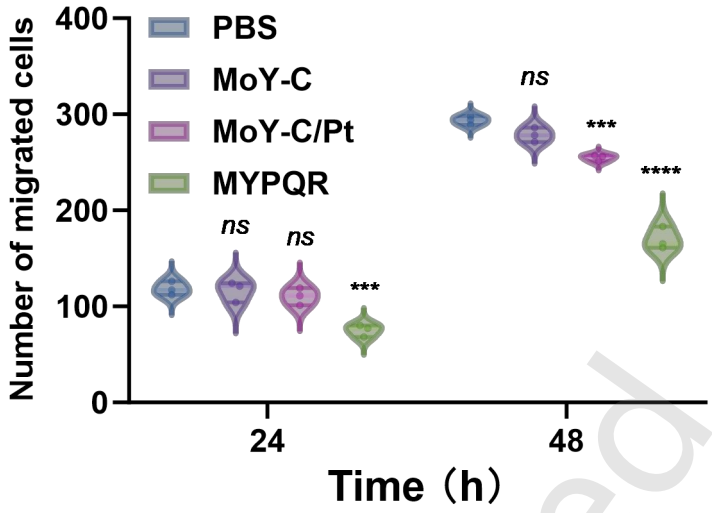


Figure S13. Effect of different materials on cell migration ability.

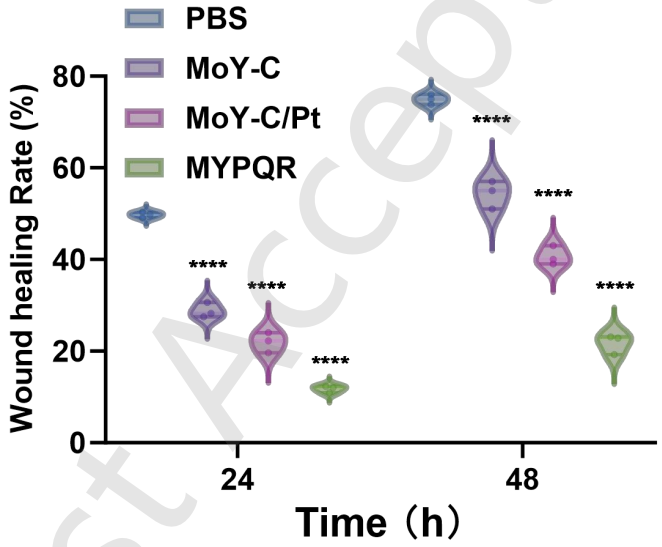


Figure S14. Effect of different materials on wound healing rate.

Just Accepted

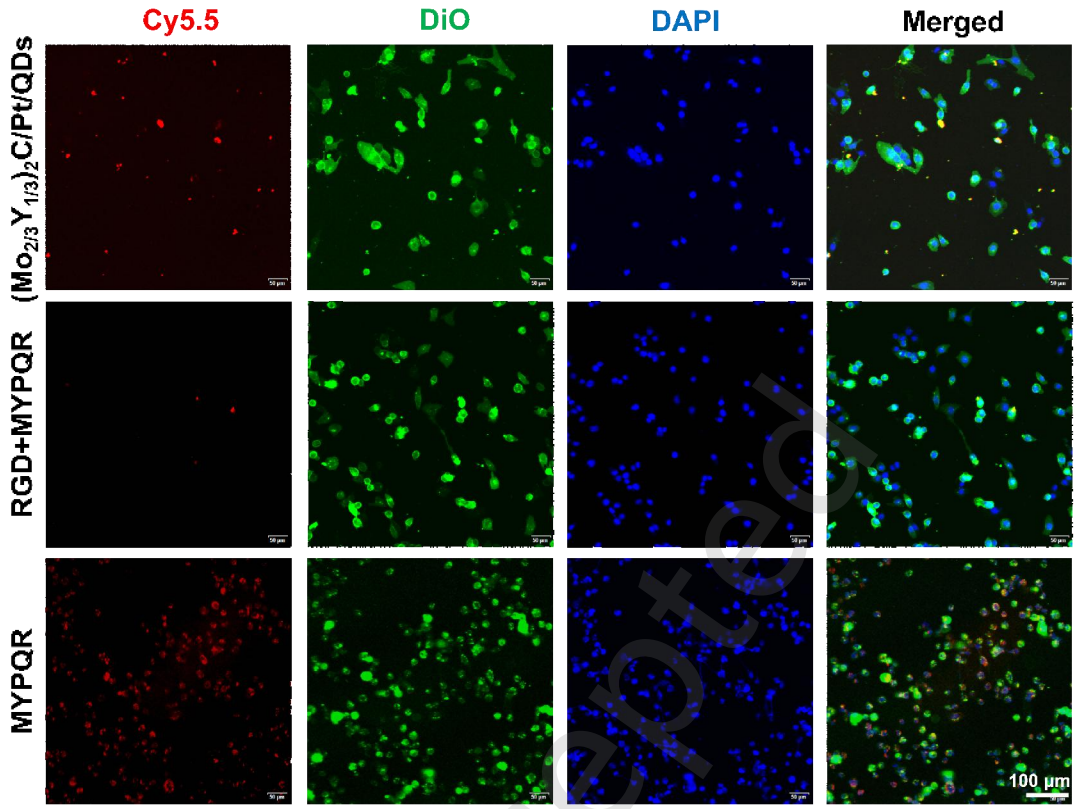


Figure S15. CLSM evaluation of cellular uptake and RGD-targeting specificity in HCC-LM3 cells.

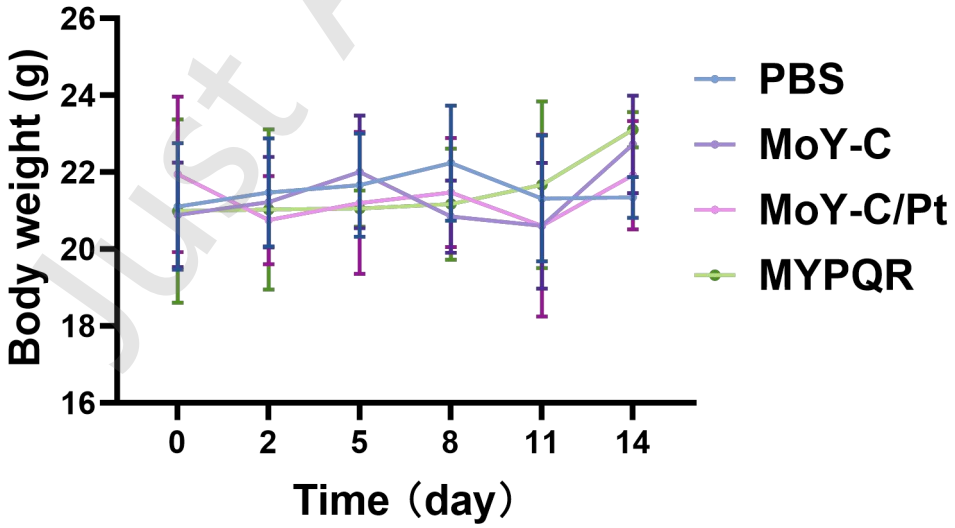


Figure S16. Body weight variations monitored in mice across each treatment group to assess systemic toxicity.

Just Accepted

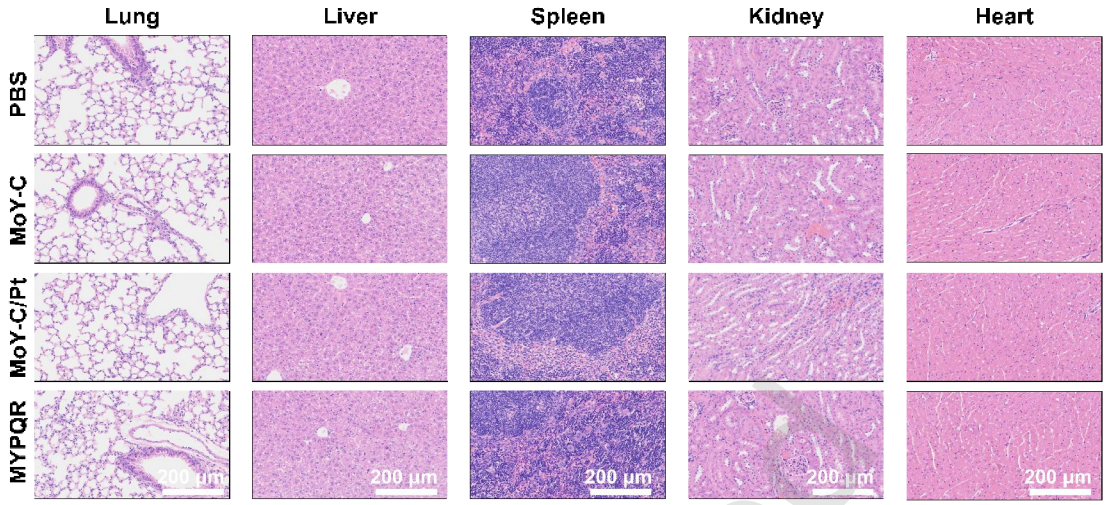


Figure S17. Histopathological evaluation of major organs after treatment with different materials.

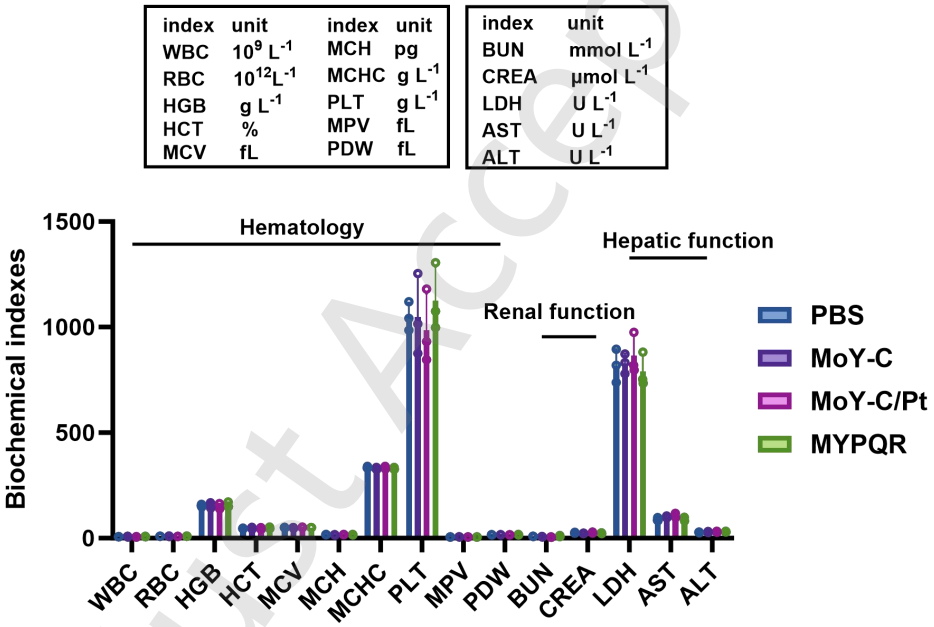


Figure S18. Routine hematology and serum biochemistry evaluation.

Just Accepted